ATLAS CONF Note

ATLAS-CONF-2018-041

24th July 2018

Search for supersymmetry in final states with missing transverse momentum and multiple b-jets in proton–proton collisions at $\sqrt{s} = 13$ TeV with the ATLAS detector

The ATLAS Collaboration

A search for supersymmetry involving the pair production of gluinos decaying via third-generation squarks into the lightest neutralino ($\tilde{\chi}_1^0$) is reported. It uses LHC proton–proton collision data at a centre-of-mass energy $\sqrt{s} = 13$ TeV with an integrated luminosity of 79.8 fb^{-1} collected with the ATLAS detector from 2015 to 2017. The search is performed in events containing large missing transverse momentum and several energetic jets, at least three of which must be identified as containing b-quarks. No excess is found above the predicted background. For $\tilde{\chi}_1^0$ masses below approximately 800 GeV, gluino masses of less than 2.2 TeV are excluded at 95% confidence level in simplified models involving the pair production of gluinos that decay via top or bottom squarks. An interpretation of the limits in terms of the branching ratios of the gluinos into third-generation squarks is also provided.

ATLAS-CONF-2018-041
25 July 2018

© 2018 CERN for the benefit of the ATLAS Collaboration.
Reproduction of this article or parts of it is allowed as specified in the CC-BY-4.0 license.

1 Introduction

Supersymmetry (SUSY) [1–6] is a generalisation of space-time symmetries that predicts new bosonic partners for the fermions and new fermionic partners for the bosons of the Standard Model (SM). In SUSY models, if R-parity is conserved [7], SUSY particles are produced in pairs and the lightest supersymmetric particle (LSP) is stable. The scalar partners of the left- and right-handed quarks, the squarks $\tilde{q}_{\mathrm{L}}$ and $\tilde{q}_{\mathrm{R}}$, can mix to form two mass eigenstates $\tilde{q}_1$ and $\tilde{q}_2$, ordered by increasing mass. SUSY can solve the hierarchy problem [8–11] by reducing unnatural tuning in the Higgs sector by orders of magnitude, provided that the superpartners of the top quark (the top squarks, $\tilde{t}_{\mathrm{L}}$ and $\tilde{t}_{\mathrm{R}}$) have masses not too far above the weak scale [12]. Because of the SM weak-isospin symmetry, the mass of the lightest bottom squark $\tilde{b}_1$ is also expected to be close to the weak scale. The fermionic partners of the gluons, the gluinos ($\tilde{g}$), are also motivated by naturalness [13] to have a mass around the TeV scale in order to limit their contributions to the radiative corrections to the top squark masses. For these reasons, and because the gluinos are expected to be pair-produced with a high cross-section at the Large Hadron Collider (LHC), the search for gluino production with decays via top and bottom squarks is highly motivated at the LHC.

This note presents a search for pair-produced gluinos decaying via top or bottom squarks in events with multiple jets containing b-quarks (b-jets in the following), high missing transverse momentum of magnitude $E_{\mathrm{T}}^{\mathrm{miss}}$, and potentially additional light-quark jets and/or an isolated charged lepton.[1] Interpretations are provided in the context of several simplified models [14–16] probing various gluino decays into third-generation squarks and the LSP. The latter is assumed to be the lightest neutralino $\tilde{\chi}_1^0$, a linear superposition of the superpartners of the neutral electroweak and Higgs bosons. One model also features the lightest charginos $\tilde{\chi}_1^{\pm}$, which are linear superpositions of the superpartners of the charged electroweak and Higgs bosons. Several benchmark scenarios which were studied in the earlier instances of this analysis [17] are considered: two models, known as "Gtt" and "Gbb" respectively and a third model with variable gluino branching ratios to $\tilde{g} \to b\bar{b}\tilde{\chi}_1^0$, $\tilde{g} \to t\bar{b}\tilde{\chi}_1^-$ and $\tilde{g} \to t\bar{t}\tilde{\chi}_1^0$. These are depicted in Figures 1 and 2. Pair-produced gluinos with top-squark-mediated decays have also been searched for using events containing pairs of same-sign leptons or three leptons using 13 TeV data [18, 19]. The same-sign/three lepton search is comparable in sensitivity to the search presented in this note only when the masses of the gluino and the LSP are very close to each other. Similar searches performed using the 13 TeV dataset by the CMS experiment have produced results comparable to the ATLAS searches [20–23].

The results presented in this note are an update of the ones obtained using 36.1 fb^{-1} of data [17] with the same analysis strategy and selection criteria, but an extended dataset that consists of 79.8 fb^{-1} of proton–proton (pp) collision data collected with the ATLAS detector [24] at a centre-of-mass energy of 13 TeV.

[1] The term "lepton" refers exclusively to an electron or a muon in this note.

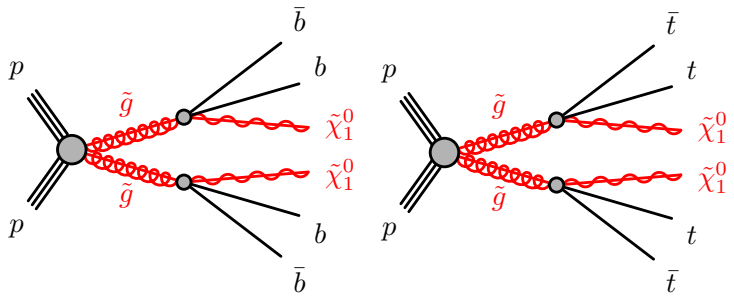

Figure 1: The decay topologies in the (a) Gbb and (b) Gtt simplified models.

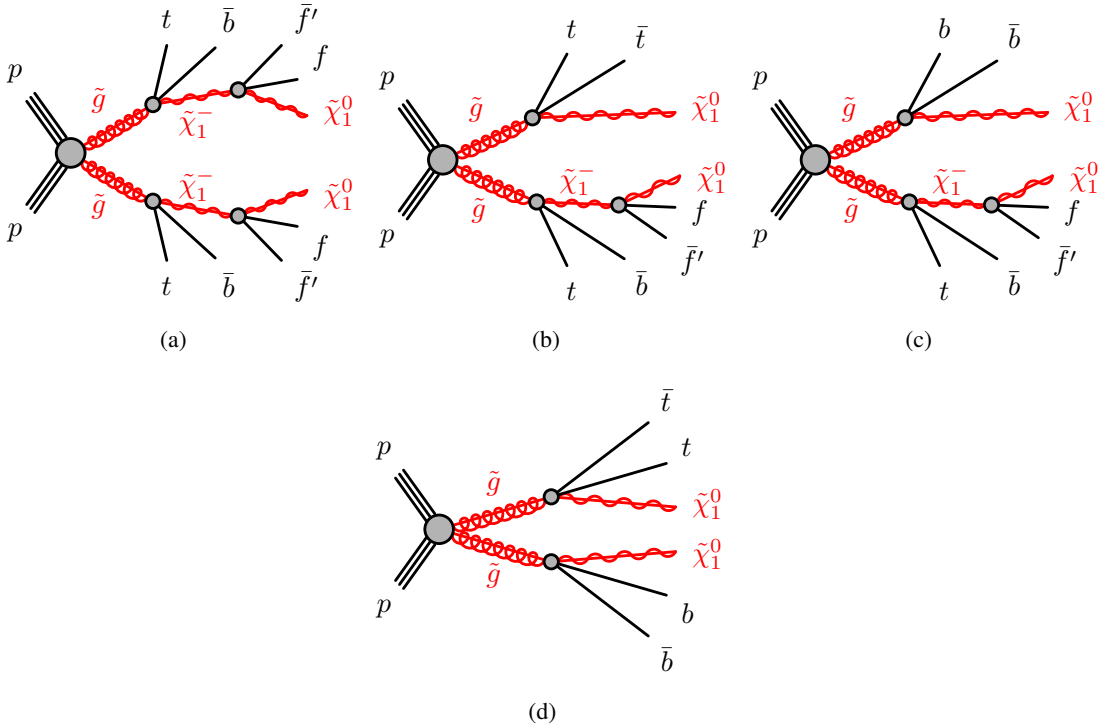

Figure 2: The additional decay topologies of the variable gluino branching ratio model in addition to the ones of Figure 1. (a) Both gluinos can decay as $\tilde{g} \to t\bar{b}\tilde{\chi}_1^-$ with $\tilde{\chi}_1^- \to f\bar{f}'\tilde{\chi}_1^0$, or only one can with the other decaying as (b) $\tilde{g} \to t\bar{t}\tilde{\chi}_1^0$ or (c) $\tilde{g} \to b\bar{b}\tilde{\chi}_1^0$. (d) Finally, one gluino can decay as $\tilde{g} \to t\bar{t}\tilde{\chi}_1^0$ and the other as $\tilde{g} \to b\bar{b}\tilde{\chi}_1^0$. The charge conjugate processes are implied. The fermions originating from the $\tilde{\chi}_1^\pm$ decay have low momentum and are not detected because the mass difference between the $\tilde{\chi}_1^\pm$ and the $\tilde{\chi}_1^0$ is fixed to 2 GeV.

2 ATLAS detector

The ATLAS detector is a multipurpose particle physics detector with a forward-backward symmetric cylindrical geometry and nearly 4π coverage in solid angle.[2] The inner tracking detector (ID) consists of silicon pixel and microstrip detectors covering the pseudorapidity region $|\eta| < 2.5$, surrounded by a transition radiation tracker, which enhances electron identification in the region $|\eta| < 2.0$. Before the start of Run 2, the new innermost pixel layer, the insertable B-layer (IBL) [25], was inserted at a mean sensor radius of 3.3 cm. The ID is surrounded by a thin superconducting solenoid providing an axial 2 T magnetic field and by a fine-granularity lead/liquid-argon (LAr) electromagnetic calorimeter covering $|\eta| < 3.2$. A steel/scintillator-tile calorimeter provides coverage for hadronic showers in the central pseudorapidity range ($|\eta| < 1.7$). The endcaps ($1.5 < |\eta| < 3.2$) of the hadronic calorimeter are made of LAr active layers with copper as the absorber material. The forward region ($3.1 < |\eta| < 4.9$) is instrumented with a LAr calorimeter for both the EM and hadronic measurements. A muon spectrometer with an air-core toroidal magnet system surrounds the calorimeters. Three layers of high-precision tracking chambers provide coverage in the range $|\eta| < 2.7$, while dedicated fast chambers allow triggering in the region $|\eta| < 2.4$. The ATLAS trigger system [26] consists of a hardware-based level-1 trigger followed by a software-based high-level trigger (HLT).

3 Data and simulated event samples

The data used in this analysis were collected by the ATLAS detector from pp collisions produced by the LHC at a centre-of-mass-energy of 13 TeV and 25 ns proton bunch spacing over the 2015, 2016 and 2017 data-taking periods. The full dataset corresponds to an integrated luminosity of 79.8 fb^{-1} after the application of beam, detector and data-quality requirements.

Events are required to pass an $E_{\mathrm{T}}^{\mathrm{miss}}$ trigger with thresholds of 70 GeV, 100 GeV and 110 GeV at the HLT level for the 2015, early 2016 and late 2016/2017 datasets, respectively. These triggers are fully efficient for events passing the preselection defined in Section 5, which requires the offline reconstructed $E_{\mathrm{T}}^{\mathrm{miss}}$ to exceed 200 GeV. There are on average 32 inelastic pp collisions per bunch crossing (the interactions other than the hard scatter are referred to as "pile-up") in the dataset.

Samples of Monte Carlo (MC) simulated events are used to model the signal and background processes in this analysis, except multijet processes, which are estimated using a data-driven method (see Section 5). The MC simulated events strategy is largely similar to the one in Ref. [17], and the summary of the generators can be found in Table 1.

The most notable change concerns the modelling of the dominant background in the signal regions such as the production of $t\bar{t}$ pairs with additional high transverse momentum (p_{T}) jets. It is simulated using the Powheg-Box [27] v2 event generator using the NNPDF3.0 [28] PDF set. The parton shower, fragmentation, and the underlying event are simulated using Pythia v8.230 [29]. The h_{damp} parameter in Powheg, which controls the p_{T} of the first additional emission beyond the Born level and thus regulates

[2] ATLAS uses a right-handed coordinate system with its origin at the nominal interaction point in the centre of the detector. The positive x-axis is defined by the direction from the interaction point to the centre of the LHC ring, with the positive y-axis pointing upwards, while the beam direction defines the z-axis. Cylindrical coordinates (r, ϕ) are used in the transverse plane, ϕ being the azimuthal angle around the z-axis. The pseudorapidity η is defined in terms of the polar angle θ by $\eta = -\ln\tan(\theta/2)$. Rapidity is defined as $y = 0.5\ln[(E + p_z)/(E - p_z)]$ where E denotes the energy and p_z is the component of the momentum along the beam direction.

the p_{T} of the recoil emission against the $t\bar{t}$ system, is set to 1.5 times the mass of the top quark (m_{top} = 172.5 GeV).

Other changes in generator settings for the modelling of small background sources were found not to affect significantly the sensitivity of this analysis. All background simulated processes are normalised using the best available theoretical calculation for their respective cross sections.

The signal samples are normalised using the best cross-section calculations at NLO in the strong coupling constant, adding the resummation of soft gluon emission at the next-to-leading-logarithm (NLL) accuracy [30–34]. The mass difference between the $\tilde{\chi}_1^{\pm}$ and the $\tilde{\chi}_1^0$ is fixed to 2 GeV. The nominal cross section and the uncertainty are taken from an envelope of cross section predictions using different PDF sets and factorisation and renormalisation scales, as described in Ref. [35].

Process	Generator + fragmentation/hadronization	Tune	PDF set	Cross-section order
Gbb/Gtb/Gtt	MadGraph5_aMC@NLO-2.2.2 + Pythia v8.186	A14	NNPDF2.3	NLO+NLL [30–35]
$t\bar{t}$	Powheg-Box v2 + Pythia-8.230	A14	NNPDF3.0	NNLO+NNLL [36]
Single top Wt-channel (s/t)	Powheg-Box v1 (v2) + Pythia-6.428 (-8.230)	PERUGIA2012	CT10	NNLO+NNLL [37–39]
$t\bar{t}W/t\bar{t}Z$	MadGraph5_aMC@NLO-2.2.2 + Pythia-8.186	A14	NNPDF2.3	NLO [40]
4-tops	MadGraph-2.2.2 + Pythia-8.186	A14	NNPDF2.3	NLO [40]
$t\bar{t}H$	MadGraph5_aMC@NLO-2.2.1 + Herwig++-2.7.1	UEEE5	CT10	NLO [41]
Dibosons WW, WZ, ZZ	Sherpa-2.2.1	Default	NNPDF3.0	NLO [42, 43]
W/Z+jets	Sherpa-2.2.1	Default	NNPDF3.0	NNLO [44]

Table 1: List of generators used for the different processes. Information is given about the tuned set of underlying event and hadronisation parameters (Tune), the PDF sets and the perturbative QCD highest-order accuracy used for the normalization of the different samples.

4 Event reconstruction

The data considered in this analysis were taken in stable beam conditions and satisfy detector and data-quality requirements. Events are required to have a reconstructed primary vertex with at least two associated tracks with $p_{\mathrm{T}} > 0.4$ GeV, consistent with the beamspot envelope. If multiple primary vertices are reconstructed, the one with the highest sum of the p_{T}^2 of the associated tracks is selected as the primary vertex [45].

Electron candidates are reconstructed from energy clusters in the electromagnetic calorimeter and inner detector tracks [46]. They are required to satisfy a set of "loose" identification criteria [47], and have p_{T} > 20 GeV and $|\eta| < 2.47$. The track associated with the electron candidate must have an impact parameter evaluated at the point of the closest approach between the track and the beam axis in the longitudinal plane (z_0) that satisfies $|z_0 \sin\theta| < 0.5$ mm.[3] Muon candidates are reconstructed from matching tracks in the inner detector and muon spectrometer. They are required to meet "medium" identification requirements [48], and have $p_{\mathrm{T}} > 20$ GeV, $|\eta| < 2.5$. As is done for electrons, a value of $|z_0 \sin\theta| < 0.5$ mm is required for muons. In addition, events containing one or more muon candidates for which the transverse impact parameter (d_0) is larger than 0.2 mm or $|z_0| > 1$ mm are rejected to suppress muons coming from cosmic rays.

Candidate jets are reconstructed from three-dimensional topological energy clusters [49] in the calorimeter using the anti-k_t jet algorithm [50, 51] with a radius parameter of 0.4 (small-R jets). A calibration is applied [52] and additional criteria are required to reject jets arising from non-collisions sources or detector noise [53] and to reject jets that originate from pile-up [54]. Candidate jets are required to have $p_{\mathrm{T}} > 20$ GeV and $|\eta| < 2.8$. After resolving overlaps with electrons and muons, selected jets are required to satisfy the stricter requirement of $p_{\mathrm{T}} > 30$ GeV.

A jet is tagged as a b-jet candidate by means of a multivariate algorithm using information about the impact parameters of inner detector tracks matched to the jet, the presence of displaced secondary vertices, and the reconstructed flight paths of b- and c-hadrons inside the jet [55, 56]. The algorithm is used at a working point providing an efficiency of 77%, as determinated in simulated $t\bar{t}$ events. This corresponds to rejection factors of 113, 4 and 16 for jets originated by light-quarks and gluons, c-quarks and τ-leptons.

Following the settings detailed in Ref. [17], overlaps between candidate objects are removed sequentially, first removing electrons or jets originating from lepton bremsstrahlung or jets coming from the showering of a prompt electron. The remaining lepton candidates are allowed to be as close as $\Delta R = 0.4$ for electrons (muons) when $E_{\mathrm{T}} < 50$ GeV ($p_{\mathrm{T}} < 50$ GeV), or $\Delta R = \min(0.4, 0.04 + 10\ \mathrm{GeV}/p_{\mathrm{T}})$ for electrons (muons) with $E_{\mathrm{T}} > 50$ GeV ($p_{\mathrm{T}} > 50$ GeV) to any other remaining jet candidate. This p_{T} dependent requirement provides high lepton selection efficiency in the high-p_{T} regime where b-jets and leptons originating from top decays become collimated.

After resolving the overlap with leptons, the candidate small-R jets are re-clustered [57] into large-R jets using the anti-k_t algorithm with a radius parameter of 0.8. The calibration from the input small-R jets propagates directly to the re-clustered jets. These re-clustered jets are then trimmed [57–60] by removing subjets whose p_{T} falls below 10% of the p_{T} of the original re-clustered jet. The resulting large-R jets are required to have $p_{\mathrm{T}} > 100$ GeV and $|\eta| < 2.0$. When it is not explicitly stated otherwise, the term "jets" in this note refers to small-R jets.

The remaining electrons and muons which survive the overlap removal are selected if they fulfill an isolation requirement based on the scalar sum of p_{T} of tracks in a cone around the lepton track. The radius of the cone depends on the p_{T} of the lepton to ensure a flat efficiency of around 99% across the whole electron transverse energy and muon transverse momentum ranges. In addition, electrons are required to satisfy the "tight" identification criteria [47], and electrons (muons) must verify $|d_0|/\sigma_{d_0} < 5$ (3) where σ_{d_0} is the measured uncertainty of d_0.

Finally, the missing transverse momentum $\vec{p}_{\mathrm{T}}^{miss}$ (with magnitude $E_{\mathrm{T}}^{\mathrm{miss}}$) is present in events with unbalanced kinematics in the transverse plane. This can originate from particles such as neutrinos or neutralinos

[3] Both the transverse and longitudinal impact parameters are defined with respect to the selected primary vertex.

escaping detection, from particles produced outside the detector acceptance, or from badly reconstructed objects or mis-measured object properties. The $E_{\mathrm{T}}^{\mathrm{miss}}$ is calculated as the magnitude of the negative vectorial sum of the p_{T} of all reconstructed and calibrated objects in the event. An additional "soft" term is added to account for the remaining energy contributions that are not associated with any reconstructed object, but are associated with the identified primary vertex. This term is calculated from inner detector tracks to make it more resilient to contamination from pile-up interactions [61, 62] .

5 Event selection

The event selection is divided in two sets of preselection criteria targeting final states which contain no leptons or at least one lepton (referred to as 0-lepton and 1-lepton channels in the following). Events are preselected by requiring that $E_{\mathrm{T}}^{\mathrm{miss}} > 200$ GeV, which ensures that the efficiency for the $E_{\mathrm{T}}^{\mathrm{miss}}$ triggers used in this analysis is close to ∼100%, and by requiring at least four jets of which at least three must be b-tagged. To enhance the sensitivity to the various signal benchmarks, multiple signal regions (SRs) are defined using the following discriminating variables. The effective mass (m_{eff}):

$$m_{\mathrm{eff}} = \sum_i p_{\mathrm{T}}^{\mathrm{jet}_i} + \sum_j p_{\mathrm{T}}^{\ell_j} + E_{\mathrm{T}}^{\mathrm{miss}},$$

where the first and second sums are over the selected jets (N_{jet}) and leptons (N_{lepton}), respectively. It typically has a much higher value in pair-produced gluino events than in background events.

In regions with at least one selected lepton, the transverse mass m_{T} composed of the p_{T} of the leading selected lepton (ℓ) and $E_{\mathrm{T}}^{\mathrm{miss}}$ is defined as:

$$m_{\mathrm{T}} = \sqrt{2p_{\mathrm{T}}^{\ell} E_{\mathrm{T}}^{\mathrm{miss}} \{1 - \cos[\Delta\phi(\vec{p}_{\mathrm{T}}^{\mathrm{miss}}, \vec{p}_{\mathrm{T}}^{\ell})]\}}.$$

It is used to reduce the $t\bar{t}$ and W+jets background events in which a W boson decays leptonically. The m_{T} distribution for these backgrounds has an upper bound corresponding to the W boson mass and typically has higher values for Gtt events. In addition, the minimum transverse mass formed by $E_{\mathrm{T}}^{\mathrm{miss}}$ and any of the three highest-p_{T} b-tagged jets in the event is used:

$$m_{\mathrm{T,min}}^{b\text{-jets}} = \min_{i \leq 3} \left(\sqrt{2p_{\mathrm{T}}^{b\text{-jet}_i} E_{\mathrm{T}}^{\mathrm{miss}} \{1 - \cos[\Delta\phi(\vec{p}_{\mathrm{T}}^{\mathrm{miss}}, \vec{p}_{\mathrm{T}}^{b\text{-jet}_i})]\}} \right).$$

The $m_{\mathrm{T,min}}^{b\text{-jets}}$ distribution has an upper bound corresponding to the top quark mass for $t\bar{t}$ events with a semileptonic top quark decay, while peaking at higher values for Gbb and Gtt events. Another powerful variable is the total jet mass variable, defined as:

$$M_J^{\Sigma} = \sum_{i \leq 4} m_{J,i},$$

where $m_{J,i}$ is the mass of the large-radius re-clustered jet i in the event. The decay products of a hadronically decaying boosted top quark are reconstructed in a single large-radius re-clustered jet, resulting in a jet

with a high mass. This variable typically has larger values for Gtt events than for background events, since Gtt events contain as many as four hadronically decaying top quarks while the background is dominated by $t\bar{t}$ events.

The requirement of a selected lepton, with the additional requirements on jets, $E_{\mathrm{T}}^{\mathrm{miss}}$ and event variables described above, makes the multijet background negligible for the $\geq$ 1-lepton signal regions. For the 0-lepton signal regions, the minimum azimuthal angle $\Delta\phi_{\mathrm{min}}^{4\mathrm{j}}$ between $\vec{p}_{\mathrm{T}}^{\mathrm{miss}}$ and the p_{T} of the four leading small-R jets in the event, defined as:

$$\Delta\phi_{\mathrm{min}}^{4\mathrm{j}} = \mathrm{min}_{i\leq 4}\left(|\phi_{\mathrm{jet}_i} - \phi_{\vec{p}_{\mathrm{T}}^{\mathrm{miss}}}|\right),$$

is required to be greater than 0.4. This requirement supresses the multijet background, which can produce events with large $E_{\mathrm{T}}^{\mathrm{miss}}$ if containing poorly measured jets or neutrinos emitted close to the axis of a jet.

A similar variable to $\Delta\phi_{\mathrm{min}}^{4\mathrm{j}}$, denoted $\Delta\phi^{\mathrm{j}_1}$, is also used in the Gbb signal regions targeting small mass differences between the gluino and the neutralino, allowing the identification of events containing a high-p_{T} jet coming from initial-state radiation (ISR) and recoiling against the gluino pair. It is defined as the absolute value of the azimuthal angle separating the p_{T} of the leading jet and $\vec{p}_{\mathrm{T}}^{\mathrm{miss}}$, and is expected to have larger values for the targeted signal than for the background.

In signal-depleted regions, discrepancies in the shapes of m_{eff}, M_J^{Σ} and $E_{\mathrm{T}}^{\mathrm{miss}}$ spectra between the preselected data and the expected background in the 1-lepton channel were found, whereas no similar discrepancies are visible in the 0-lepton channel. To account for these discrepancies, a correction factor depending on $\sum_i p_{\mathrm{T}}^{\mathrm{jet}_i} + p_{\mathrm{T}}^{\ell}$ was applied to the MC simulations. Data and simulated events are selected in a $t\bar{t}$ enriched region defined by applying 1-lepton preselection criteria and requiring exactly two b-tagged jets. Simulated events are normalised to the total number of observed events and the ratio between data and the MC events is computed as a function of $\sum_i p_{\mathrm{T}}^{\mathrm{jet}_i} + p_{\mathrm{T}}^{\ell}$. This ratio is fitted to a decreasing exponential function which is used to correct the MC simulations. The correction factors have typical values between ~1.1 and ~0.6 at low and high $\sum_i p_{\mathrm{T}}^{\mathrm{jet}_i} + p_{\mathrm{T}}^{\ell}$. Systematic uncertainties related to the quality of the fit are assigned to the correction factors. To test the dependence of the nominal correction on the physics process, the MC correction factors were estimated in W+jets and Z+jets enriched regions, and were found to agree well with each other within the uncertainty of the fit.

Figures 3 and 4 show the multiplicity of selected jets and b-tagged jets, the distributions of $E_{\mathrm{T}}^{\mathrm{miss}}$, m_{eff}, and M_J^{Σ} for events passing the 0-lepton and the 1-lepton preselection, respectively. Figure 3 (4) also displays the distribution of $m_{\mathrm{T,min}}^{b\text{-jets}}$ (m_{T}) in the 0-lepton (1-lepton) channel. The correction described above is applied in the 1-lepton channel. The uncertainty bands include the statistical and experimental systematic uncertainties, as described in Section 7, but not the theoretical uncertainties in the background modelling. The data and the predicted background are found to agree reasonably well at the preselection level after the kinematic reweighting described earlier. A discrepancy between data and prediction is observed for the number of b-tagged jets, but it has no impact on the background estimate after the normalisation of the simulation in dedicated control regions with the same b-tagged jets requirements as the signal regions. Example signal models with enhanced cross-sections are overlaid for comparison.

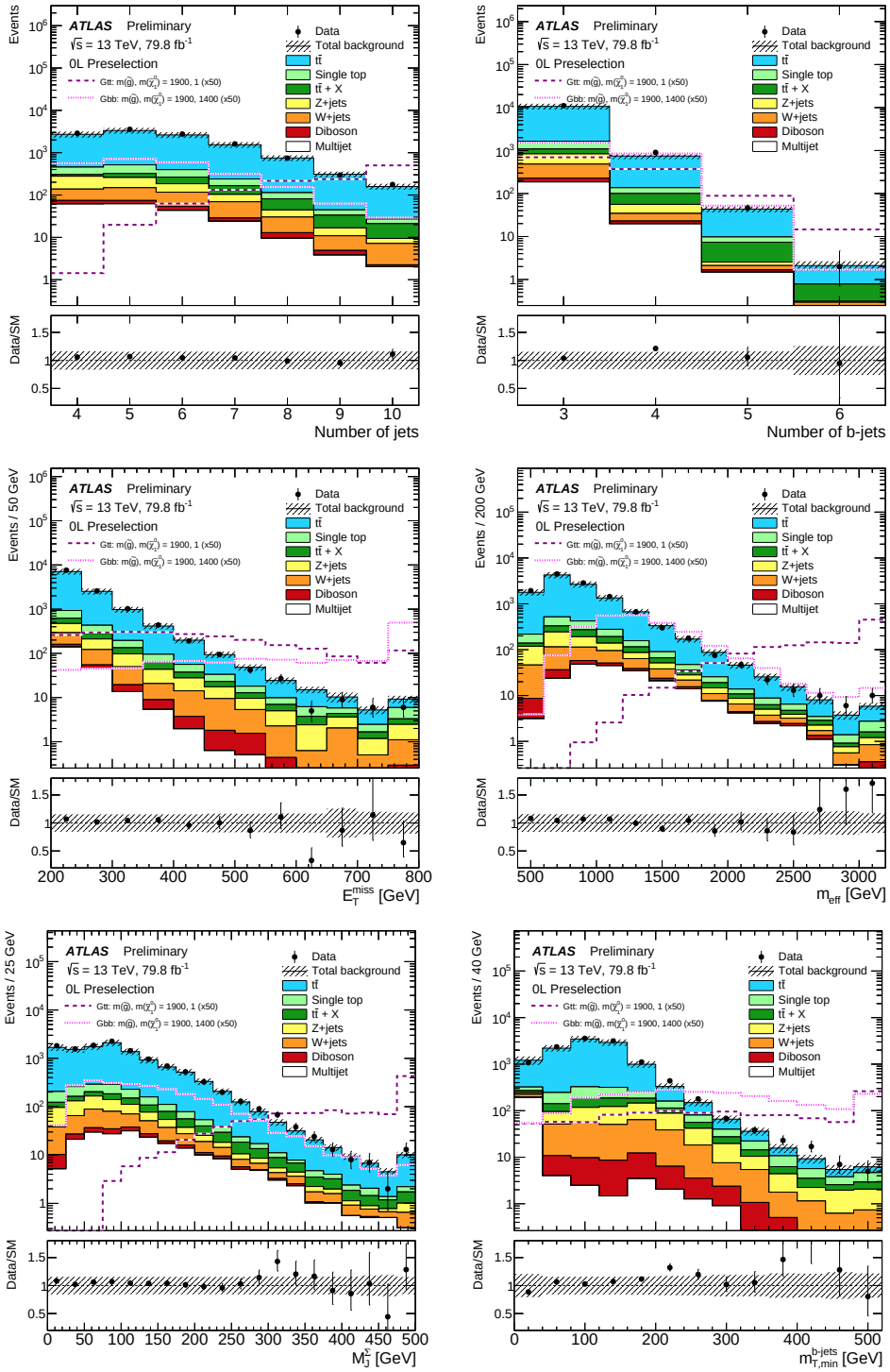

Figure 3: Distributions of (top-left) the number of selected jets (N_{jet}), (top-right) the number of selected b-tagged jets, (centre-left) $E_{\text{T}}^{\text{miss}}$, (centre-right) m_{eff}, (bottom-left) M_J^{Σ} and (bottom-right) $m_{\text{T,min}}^{b\text{-jets}}$ for events passing the 0-lepton preselection criteria. The statistical and experimental systematic uncertainties (as defined in Section 7) are included in the uncertainty band. The last bin includes overflow events. The lower part of each figure shows the ratio of data to the background prediction. All backgrounds (including $t\bar{t}$) are normalised using the best available theoretical calculation described in Section 3. The background category $t\bar{t}+X$ includes $t\bar{t}W/Z$, $t\bar{t}H$ and $t\bar{t}t\bar{t}$ events. Example signal models with cross-sections enhanced by a factor of 50 are overlaid for comparison.

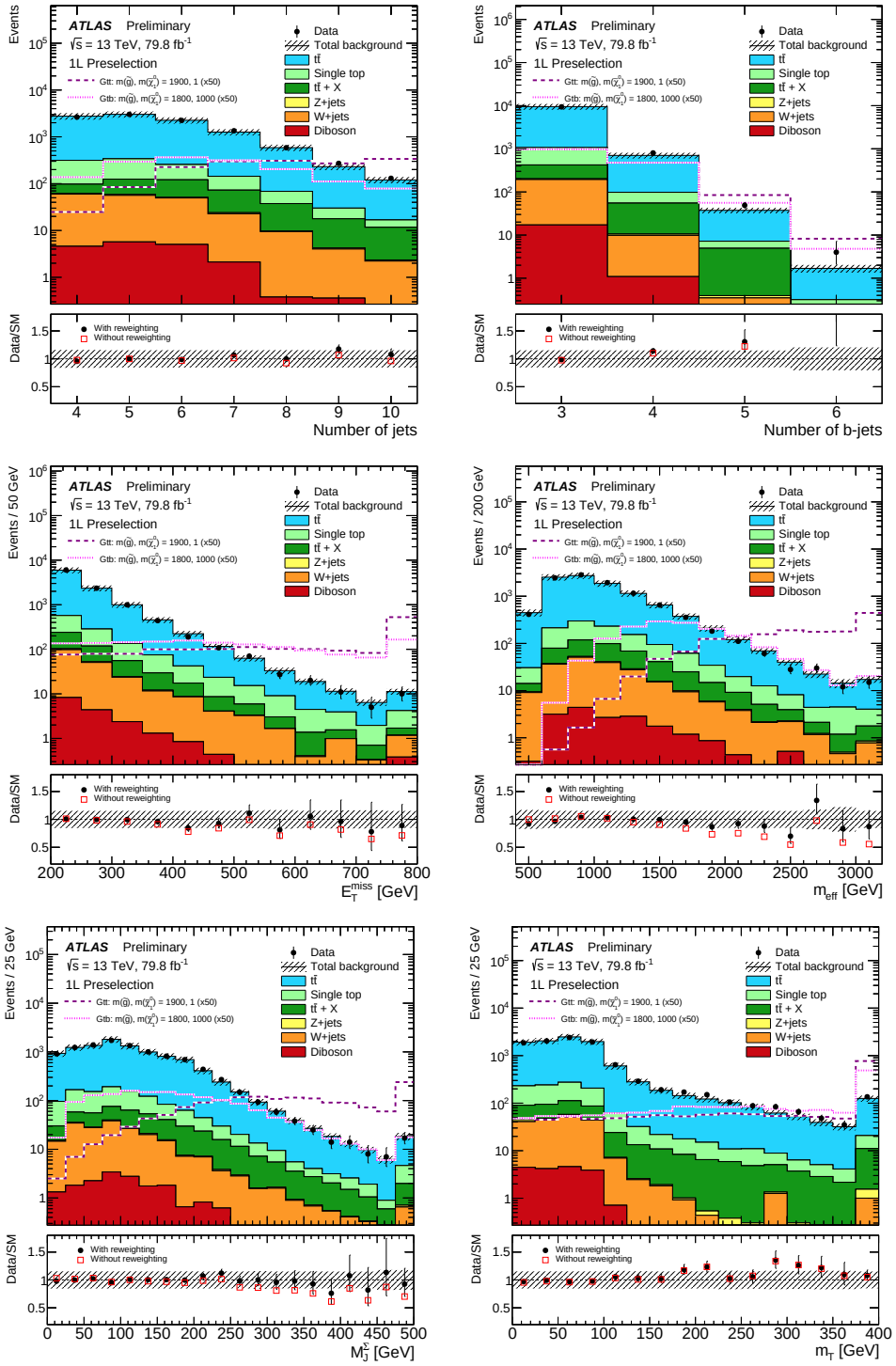

Figure 4: Distributions of (top-left) the number of selected jets (N_{jet}), (top-right) the number of selected b-tagged jets, (centre-left) $E_{\text{T}}^{\text{miss}}$, (centre-right) m_{eff}, (bottom-left) M_J^{Σ} and (bottom-right) m_{T} for events passing the 1-lepton preselection criteria, after applying the kinematic reweighting to the m_{eff} distribution described in the text. The statistical and experimental systematic uncertainties (as defined in Section 7) are included in the uncertainty band. The last bin includes overflow events. The lower part of each figure shows the ratio of data to the background prediction before (red empty squares) and after (black filled circles) the kinematic reweighting. All backgrounds (including $t\bar{t}$) are normalised using the best available theoretical calculation described in Section 3. The background category $t\bar{t} + X$ includes $t\bar{t}W/Z$, $t\bar{t}H$ and $t\bar{t}t\bar{t}$ events. Example signal models with cross-sections enhanced by a factor of 50 are overlaid for comparison.

6 Analysis strategy

The main background in all these regions is the production of a $t\bar{t}$ pair in association with heavy- and light-flavour jets. A normalisation factor for this background is extracted for each individual SR from a control region (CR) that has comparable background composition, but a much lower expected signal:background ratio. The contribution of the signal in the CR was found to be at most 6% for signal models near the edge of the exclusion sensitivity. In addition, the $t\bar{t}$ normalisation is cross-checked in validation regions (VRs) that also share a similar background composition, i.e. jet and lepton flavours, with the SR. The signal contamination in the VRs is found to be lower than 30% for benchmark signal mass points above the already excluded mass range. The $t\bar{t}$ purity is higher than 68% and 60% in the CRs and VRs, respectively. The non-$t\bar{t}$ backgrounds mainly consist of single-top, W+jets, Z+jets, $t\bar{t}+W/Z/H$, $t\bar{t}t\bar{t}$ and diboson events, which are estimated using MC simulations (Table 1). The remaining multijet background in the 0-lepton channel is estimated following the strategy of Ref. [63]. This method estimates the multijet background from a CR with the same requirements as the SR, but with the selection of $\Delta\phi^{4\text{j}}_{\text{min}}$ changed to $\Delta\phi^{4\text{j}}_{\text{min}} < 0.1$ to enhance the multijet background contribution. Then, the normalisation is extrapolated from the multijet CRs to their corresponding SRs by performing an exponential fit to the $\Delta\phi^{4\text{j}}_{\text{min}}$ distribution in the range $0 < \Delta\phi^{4\text{j}}_{\text{min}} < 0.4$. The multijet background prediction is validated by comparing data and total prediction in multijets-enhanced regions defined in ranges of $\Delta\phi^{4\text{j}}_{\text{min}}$ (such as $0.2 < \Delta\phi^{4\text{j}}_{\text{min}} < 0.3$). The contribution of the multijet background to SRs is found to be $\lesssim 2\%$. Two analysis strategies are followed, and different SR sets are defined for each, unchanged with respect to Ref. [17]:

- A **cut-and-count** analysis, using partially overlapping single-bin SRs, optimised to maximise the expected discovery power of single SRs for benchmark signal models, and allowing for reinterpretation of the results. The SRs are defined to probe the existence of a signal or to assess model-independent upper limits on the number of signal events. In the cut-and-count strategy, different regions are optimised for signals with a large mass difference between the gluino and the neutralino ($\Delta m \gtrsim 1.5$ TeV), moderate Δm ($0.3 \lesssim \Delta m \lesssim 1.5$ TeV) and small Δm ($\Delta m \lesssim 0.3$ TeV). These regions differ mainly in their kinematic selections thresholds on m_{eff}, $E_{\text{T}}^{\text{miss}}$ and M_J^{Σ} variables. For each SR, a CR is defined to constrain the $t\bar{t}$ background. In addition, VRs kinematically close to the SRs and mutually exclusive to both the CRs and SRs are used to test the $t\bar{t}$ normalisation. The definition of the VRs has not changed with respect to Ref. [17]. Background composition studies performed on simulated event samples show that semileptonic $t\bar{t}$ events, for which the lepton is outside the acceptance or is a hadronically decaying τ-lepton, dominate in the 0-lepton SRs. Thus, CRs to normalise the $t\bar{t}$+jets background make use of the 1-lepton channel, requiring the presence of exactly one signal lepton. The background prediction is checked in a 0-lepton validation region, inverting the M_J^{Σ} selection to remove any overlap with the SRs. All SR and CR definitions are given in Table 2. Only the definition of the CR targeting intermediate m_{eff} values has been changed with respect to Ref. [17]. The increased statistical precision allows the use of the same $E_{\text{T}}^{\text{miss}}$ requirement in this CR as in the corresponding VR and SR, improving the agreement between the data and expected background in the VR.

- A **multi-bin** analysis, using a set of non-overlapping SRs and CRs defined by requirements on N_{jet} and m_{eff} that are statistically combined to strengthen the exclusion limits on the targeted signal benchmarks. This set of CRs and SRs is used to exclude regions of parameter space in the various signal models. The low-N_{jet} region probes especially Gbb-like models, for which the number of hard jets is lower than in decay topologies containing top quarks. This category of events is thus only considered in the 0-lepton channel. Gtt events are mostly expected in the high-N_{jet} bin. The

intermediate jet multiplicity bin is built to be sensitive to decay topologies with a number of top quarks intermediate between Gbb and Gtt, but also to Gbb (with additional jets originating from radiation) and to Gtt (when some jets fall outside the acceptance). The m_{eff} bins are chosen to provide sensitivity to various kinematic regimes: the low-m_{eff} regions are essentially sensitive to soft signals (low Δm), while the high-m_{eff} regions are designed to select highly boosted events. For each N_{jet}–m_{eff} region, the selection was optimised over all the other variables to maximise the exclusion power for the Gbb and Gtt models. For each m_{eff} bin, a targeted range of Δm was used in the optimisation procedure. A dedicated set of regions is defined to target very compressed Gbb scenarios in which a hard ISR jet recoils against the gluino pair. This set of regions is maintained orthogonal to the other low- and intermediate-N_{jet} 0-lepton regions by requiring the leading jet not to be b-tagged and large values of $\Delta\phi^{j_1}$. A sketch of the region definition is displayed in Figure 5. All SR and CR definitions are given in Tables 3 and 4. As for the cut-and-count analysis, the definition of the VRs has not changed with respect to Ref. [17].

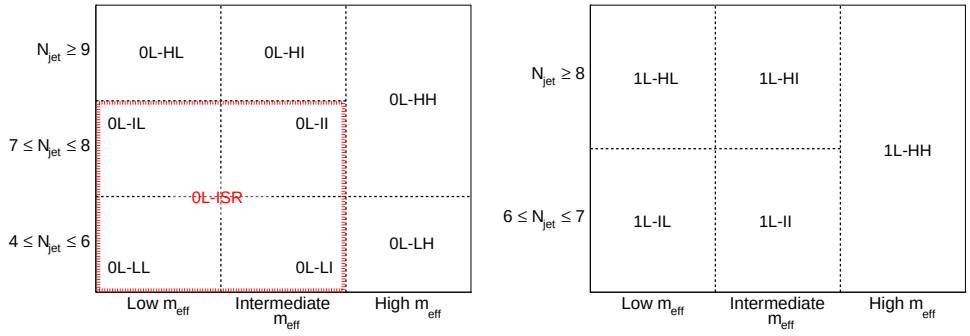

Figure 5: Scheme of the multi-bin analysis for the (left) 0-lepton and (right) 1-lepton regions. The 0L-ISR region is represented with the broad red dashed line in the left figure.

Table 2: Definitions of the Gtt SRs and CRs of the cut-and-count analysis which depend on the difference between the gluino and neutralino masses (Δm). All kinematic variables are expressed in GeV except $\Delta\phi^{4j}_{min}$, which is in radians. The $j_1 \neq b$ requirement specifies that the leading jet is not b-tagged.

Gtt 1-lepton

Criteria common to all regions: ≥ 1 signal lepton, $N_{b\text{-jets}} \geq 3$

Targeted kinematics	Type	N_{jet}	m_T	$m^{b\text{-jets}}_{T,min}$	E^{miss}_T	m^{incl}_{eff}	M^{Σ}_J
Region B (Boosted, Large Δm)	SR	≥ 5	> 150	> 120	> 500	> 2200	> 200
	CR	$= 5$	< 150	–	> 300	> 1700	> 150
Region M (Moderate Δm)	SR	≥ 6	> 150	> 160	> 450	> 1800	> 200
	CR	$= 6$	< 150	–	> 400	> 1500	> 100
Region C (Compressed, small Δm)	SR	≥ 7	> 150	> 160	> 350	> 1000	–
	CR	$= 7$	< 150	–	> 350	> 1000	–

Gtt 0-lepton

Targeted kinematics	Type	N_{lepton}	$N_{b\text{-jets}}$	N_{jet}	$\Delta\phi^{4j}_{min}$	m_T	$m^{b\text{-jets}}_{T,min}$	E^{miss}_T	m^{incl}_{eff}	M^{Σ}_J
Region B (Boosted, Large Δm)	SR	$= 0$	≥ 3	≥ 7	> 0.4	–	> 60	> 350	> 2600	> 300
	CR	$= 1$	≥ 3	≥ 6	–	< 150	–	> 275	> 1800	> 300
Region M (Moderate Δm)	SR	$= 0$	≥ 3	≥ 7	> 0.4	–	> 120	> 500	> 1800	> 200
	CR	$= 1$	≥ 3	≥ 6	–	< 150	–	> 400	> 1700	> 200
Region C (Compressed, moderate Δm)	SR	$= 0$	≥ 4	≥ 8	> 0.4	–	> 120	> 250	> 1000	> 100
	CR	$= 1$	≥ 4	≥ 7	–	< 150	–	> 250	> 1000	> 100

Gbb

Criteria common to all regions: $N_{jet} \geq 4$

Targeted kinematics	Type	N_{lepton}	$N_{b\text{-jets}}$	$\Delta\phi^{4j}_{min}$	m_T	$m^{b\text{-jets}}_{T,min}$	E^{miss}_T	m_{eff}	Others
Region B (Boosted, Large Δm)	SR	$= 0$	≥ 3	> 0.4	–	–	> 400	> 2800	–
	CR	$= 1$	≥ 3	–	< 150	–	> 400	> 2500	–
Region M (Moderate Δm)	SR	$= 0$	≥ 4	> 0.4	–	> 90	> 450	> 1600	–
	CR	$= 1$	≥ 4	–	< 150	–	> 300	> 1600	–
Region C (Compressed, small Δm)	SR	$= 0$	≥ 4	> 0.4	–	> 155	> 450	–	–
	CR	$= 1$	≥ 4	–	< 150	–	> 375	–	–
Region VC (Very Compressed, very small Δm)	SR	$= 0$	≥ 3	> 0.4	–	> 100	> 600	–	$p_T^{j_1} > 400$, $j_1 \neq b$, $\Delta\phi^{j_1} > 2.5$
	CR	$= 1$	≥ 3	–	< 150	–	> 600	–	

Table 3: Definitions of the high- and intermediate-N_{jet} SRs and CRs of the multi-bin analysis which depend on the difference between the gluino and neutralino masses (Δm). All kinematic variables are expressed in GeV except $\Delta\phi^{4\text{j}}_{\text{min}}$, which is in radians. The $\text{j}_1 = b$ ($\text{j}_1 \neq b$) requirement specifies that the leading jet is (not) b-tagged.

High-N_{jet} regions

Criteria common to all regions: $N_{b\text{-jets}} \geq 3$

Targeted kinematics	Type	N_{lepton}	$\Delta\phi^{4\text{j}}_{\text{min}}$	m_{T}	N_{jet}	$m^{b\text{-jets}}_{\text{T,min}}$	M_J^{Σ}	$E_{\text{T}}^{\text{miss}}$	m_{eff}
High-m_{eff} (HH) (Large Δm)	SR-0L	$= 0$	> 0.4	–	≥ 7	> 100	> 200	> 400	> 2500
	SR-1L	≥ 1	–	> 150	≥ 6	> 120	> 200	> 500	> 2300
	CR	≥ 1	–	< 150	≥ 6	> 60	> 150	> 300	> 2100
Intermediate-m_{eff} (HI) (Intermediate Δm)	SR-0L	$= 0$	> 0.4	–	≥ 9	> 140	> 150	> 300	$[1800, 2500]$
	SR-1L	≥ 1	–	> 150	≥ 8	> 140	> 150	> 300	$[1800, 2300]$
	CR	≥ 1	–	< 150	≥ 8	> 60	> 150	> 200	$[1700, 2100]$
Low-m_{eff} (HL) (Small Δm)	SR-0L	$= 0$	> 0.4	–	≥ 9	> 140	–	> 300	$[900, 1800]$
	SR-1L	≥ 1	–	> 150	≥ 8	> 140	–	> 300	$[900, 1800]$
	CR	≥ 1	–	< 150	≥ 8	> 130	–	> 250	$[900, 1700]$

Intermediate-N_{jet} regions

Criteria common to all regions: $N_{b\text{-jets}} \geq 3$

Targeted kinematics	Type	N_{lepton}	$\Delta\phi^{4\text{j}}_{\text{min}}$	m_{T}	N_{jet}	$\text{j}_1 = b$ or $\Delta\phi^{\text{j}_1} \leq 2.9$	$m^{b\text{-jets}}_{\text{T,min}}$	M_J^{Σ}	$E_{\text{T}}^{\text{miss}}$	m_{eff}
Intermediate-m_{eff} (II) (Intermediate Δm)	SR-0L	$= 0$	> 0.4	–	$[7, 8]$	✓	> 140	> 150	> 300	$[1600, 2500]$
	SR-1L	≥ 1	–	> 150	$[6, 7]$	–	> 140	> 150	> 300	$[1600, 2300]$
	CR	≥ 1	–	< 150	$[6, 7]$	✓	> 100	> 150	> 300	$[1600, 2100]$
Low-m_{eff} (IL) (Low Δm)	SR-0L	$= 0$	> 0.4	–	$[7, 8]$	✓	> 140	–	> 300	$[800, 1600]$
	SR-1L	≥ 1	–	> 150	$[6, 7]$	–	> 140	–	> 300	$[800, 1600]$
	CR	≥ 1	–	< 150	$[6, 7]$	✓	> 130	–	> 300	$[800, 1600]$

Table 4: Definitions of the low-N_{jet} and ISR SRs and CRs of the multi-bin analysis which depend on the difference between the gluino and neutralino masses (Δm). All kinematic variables are expressed in GeV except $\Delta\phi^{4\text{j}}_{\text{min}}$, which is in radians. The $\text{j}_1 = b$ ($\text{j}_1 \neq b$) requirement specifies that the leading jet is (not) b-tagged.

Low-N_{jet} regions

Criteria common to all regions: $N_{b\text{-jets}} \geq 3$

Targeted kinematics	Type	N_{lepton}	$\Delta\phi^{4\text{j}}_{\text{min}}$	m_{T}	N_{jet}	$\text{j}_1 = b$ or $\Delta\phi^{\text{j}_1} \leq 2.9$	$p_{\text{T}}^{\text{j}_4}$	$m^{b\text{-jets}}_{\text{T,min}}$	$E_{\text{T}}^{\text{miss}}$	m_{eff}
High-m_{eff} (LH)	SR	= 0	> 0.4	–	[4, 6]	–	> 90	–	> 300	> 2400
(Large Δm)	CR	≥ 1	–	< 150	[4, 5]	–	-	–	> 200	> 2100
Intermediate-m_{eff} (LI)	SR	= 0	> 0.4	–	[4, 6]	✓	> 90	> 140	> 350	[1400, 2400]
(Intermediate Δm)	CR	≥ 1	–	< 150	[4, 5]	✓	> 70	–	> 300	[1400, 2000]
Low-m_{eff} (LL)	SR	= 0	> 0.4	–	[4, 6]	✓	> 90	> 140	> 350	[800, 1400]
(Low Δm)	CR	≥ 1	–	< 150	[4, 5]	✓	> 70	–	> 300	[800, 1400]

ISR regions

Criteria common to all regions: $N_{b\text{-jets}} \geq 3$, $\Delta\phi^{\text{j}_1} > 2.9$, $p_{\text{T}_1}^{\text{j}} > 400$ GeVand $\text{j}_1 \neq b$

Type	N_{lepton}	$\Delta\phi^{4\text{j}}_{\text{min}}$	m_{T}	N_{jet}	$m^{b\text{-jets}}_{\text{T,min}}$	$E_{\text{T}}^{\text{miss}}$	m_{eff}
SR	= 0	> 0.4	–	[4, 8]	> 100	> 600	< 2200
CR	≥ 1	–	< 150	[4, 7]	–	> 400	< 2000

7 Systematic uncertainties

The uncertainty in the combined 2015-2017 integrated luminosity is 2.0%. It is derived, following a methodology similar to that detailed in Ref. [64], from calibrations of the luminosity scale using x–y beam-separation scans performed in August 2015, May 2016 and July 2017 (the results for 2017 are preliminary). This uncertainty affects the normalisation of all processes modelled using MC event samples.

The detector-related systematic uncertainties affect both the background estimate and the signal yield. The largest sources of the experimental uncertainties are related to the jet energy scale and resolution (JER) [52] and the b-tagging efficiencies and mistagging rates [56, 65]. The jet energy-related uncertainties are also propagated to the re-clustered large-R jets, which use them as inputs. The jet mass scale and resolution uncertainties have a negligible impact on the re-clustered jet mass. The impact of the JES uncertainties on the expected background yields is between 0.5% and 15%, while JER uncertainties affect the background yields by approximately 1–19% in the various regions. Uncertainties in the measured b-tagging efficiencies and mistagging rates are the subleading sources of experimental uncertainty. The impact of these uncertainties on the expected backgrounds yields is 1–7% depending on the considered region.

The experimental uncertainties due to different reconstruction, identification and isolation efficiencies of leptons in data compared to simulation [47, 48] are also taken into account, as well as the uncertainties in lepton energy measurements [46]. These uncertainties have a negligible impact on the final results. All lepton and jet measurement uncertainties are propagated to the calculation of $E_{\mathrm{T}}^{\mathrm{miss}}$, and additional uncertainties are included in the scale and resolution of the soft term [66]. The overall impact of the $E_{\mathrm{T}}^{\mathrm{miss}}$ soft-term uncertainties is also small.

Hadronisation and parton showering model uncertainties of the $t\bar{t}$ background are evaluated by comparing two samples generated with Powheg and showered by either Herwig++ v2.7.1 or Pythia v6.428 [17]. In addition, systematic uncertainties in the modelling of initial- and final-state radiation are explored with Powheg samples showered with two alternative settings of Pythia v6.428 [67]. The uncertainty due to the choice of matrix-element event generator is estimated by comparing the expected yields obtained using $t\bar{t}$ samples generated with MadGraph5_aMC@NLO and Powheg. The total theoretical uncertainty in the $t\bar{t}$ background estimation is taken as the sum in quadrature of these individual components. Moreover, an additional uncertainty is assigned to the fraction of $t\bar{t}$ events produced in association with additional heavy-flavour jets [17] (i.e. $t\bar{t}+ \geq 1b$ and $t\bar{t}+ \geq 1c$).

Modelling uncertainties affecting the single-top process arise especially from the interference between the $t\bar{t}$ and Wt processes. This uncertainty is estimated using inclusive $WWbb$ events, generated using MadGraph5_aMC@NLO, which are compared with the sum of $t\bar{t}$ and Wt processes. Furthermore, as in the $t\bar{t}$ modelling uncertainties, variations of Pythia v6.428 settings increasing or decreasing the amount of radiation are also used. An additional 5% uncertainty is included in the cross-section of single-top processes [68]. Overall, the modelling uncertainties affecting the single-top process lead to changes of approximately 4–35% in total yields in the various regions.

Uncertainties related to factorisation and renormalisation scales and affecting the matching procedure between the matrix element and parton shower in the W/Z+jets backgrounds are also taken into account [17]. The resulting uncertainties in the total yield range from approximately 0 to 50% in the various regions. Furthermore, a 50% uncertainty is assigned to $t\bar{t} + W/Z/H$, $t\bar{t}t\bar{t}$ and diboson backgrounds, and is assumed uncorrelated across all bins. It is found to have no significant impact on the sensitivity of

this analysis [17]. The effect of the uncertainties related to the parton distribution functions affect the background yields by <2%, and therefore are neglected here. Uncertainties due to the limited number of events in the MC background samples are included and reach up to 20% in regions targeting large mass-splitting.

A systematic uncertainty is also assigned to the kinematic correction by propagating the error of the parameters of the fit function to the correction factor. This uncertainty is applied to all background simulated samples for the 1-lepton channel.

The uncertainties in the cross-sections of signal processes are determined from an envelope of different cross-section predictions, as described in Section 3.

8 Results

The expected SM background is predicted separately in each SR with a profile likelihood fit [69] implemented in the HistFitter framework [70], referred to as a background-only fit. The fit uses as a constraint the observed event yield in the associated CR to adjust the $t\bar{t}$ normalisation, assuming that no signal contributes to this yield, and applies that normalisation factor to the number of $t\bar{t}$ events predicted by simulation in the SR. The values of the normalisation factors range from 0.7 to 1.2 depending on the CRs (see Fig. 6).

The inputs to the background-only fit for each SR are the number of events observed in its associated CR and the number of events predicted by simulation in the SR and CR for all background processes. The numbers of observed and predicted events in each CR are described by Poisson probability density functions. The systematic uncertainties in the expected values are included in the fit as nuisance parameters. They are constrained by Gaussian or log-normal distributions with widths corresponding to the sizes of the uncertainties and are treated as correlated, when appropriate, between the various regions. The product of the various probability density functions forms the likelihood, which the fit maximises by adjusting the $t\bar{t}$ normalisation and the nuisance parameters. The results of the fit are extrapolated to validation regions, following the definitions of Ref. [17], and the agreement in the validation regions is found to be good, validating further the overall fit strategy. The comparison of the observed and expected yields in the VRs after the fit is shown in Fig. 7 for the cut-and-count and the multi-bin analyses, respectively. The MC reweighting allows to improve the agreement between the observed and expected yields in the VRs. The variation of the predicted yields in the VRs due to the MC reweighting is typically < 5% and 10-30% for 1-lepton and 0-lepton channels, respectively.

The event yields in the SRs for the cut-and-count and multi-bin analyses are presented in Figure 8, where the pull is shown for each region in the lower panel. No significant excess is found above the predicted background. The background is dominated by $t\bar{t}$ events in all SRs. The subdominant background contributions in the 0-lepton regions are $Z(\rightarrow \nu\nu)$+jets and $W(\rightarrow \ell\nu)$+jets events, where for W+jets events the lepton is an unidentified electron or muon or a hadronically decaying τ-lepton. In the 1-lepton SRs, the subdominant backgrounds are single-top, $t\bar{t}W$ and $t\bar{t}Z$.

Table 5 shows the observed number of events and predicted number of background events from the background-only fit in the Gtt 1-lepton, Gtt 0-lepton and Gbb regions for the cut-and-count analysis.

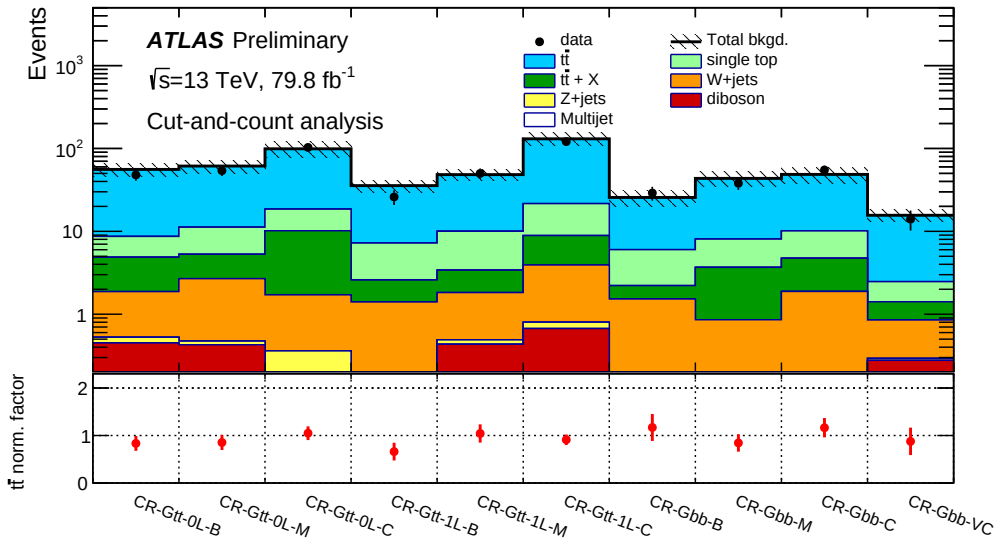

(a)

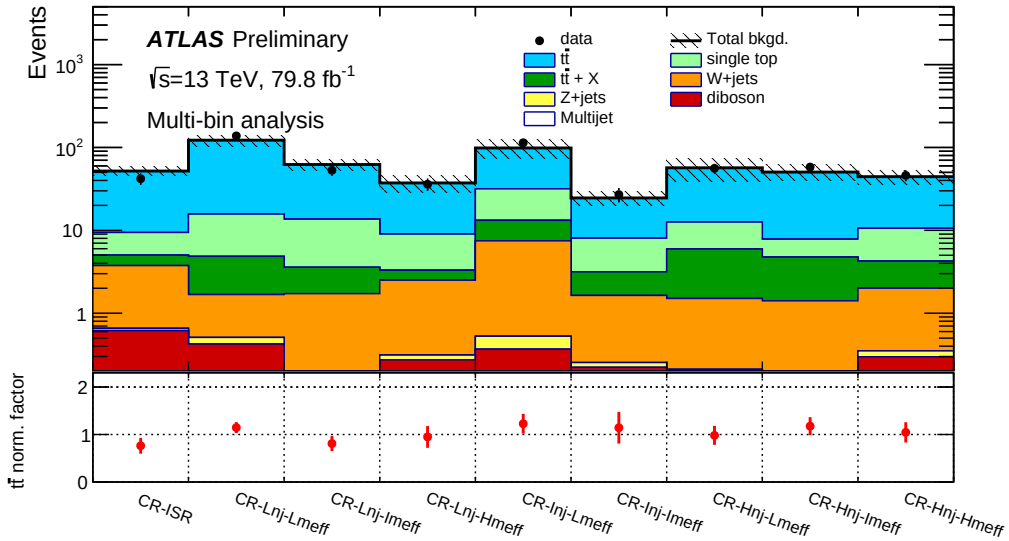

(b)

Figure 6: Pre-fit event yield in control regions and related $t\bar{t}$ normalization factors after the background-only fit for (a) the cut-and-count and (b) the multi-bin analyses. The upper panel shows the observed number of events and the predicted background yield before the fit. The background category $t\bar{t}+X$ includes $t\bar{t}W/Z$, $t\bar{t}H$ and $t\bar{t}t\bar{t}$ events. All of these regions require at least one signal lepton, for which the multijet background is negligible. All uncertainties describes in Section 7 are included in the uncertainty band. The $t\bar{t}$ normalisation is obtained from the fit and is displayed in the bottom panel.

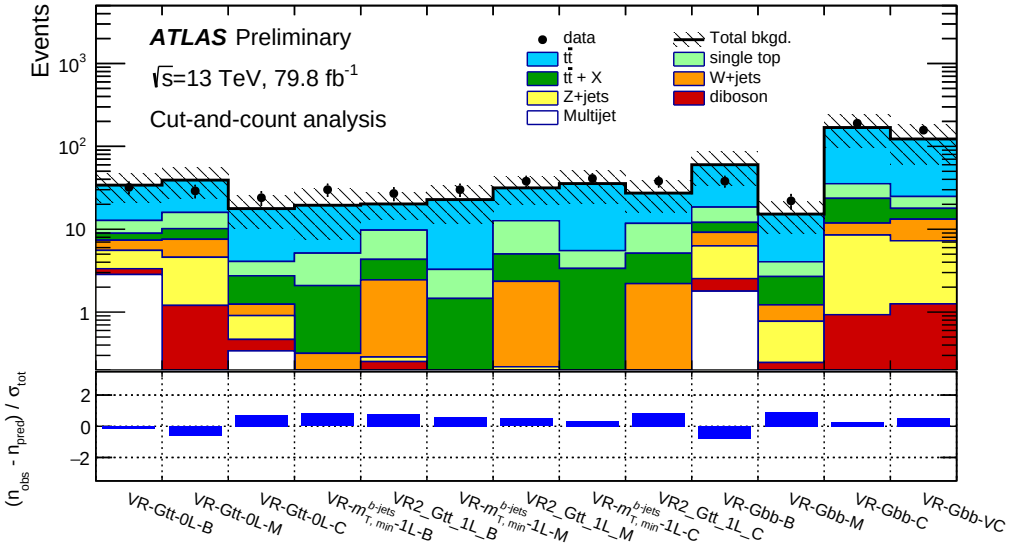

(a)

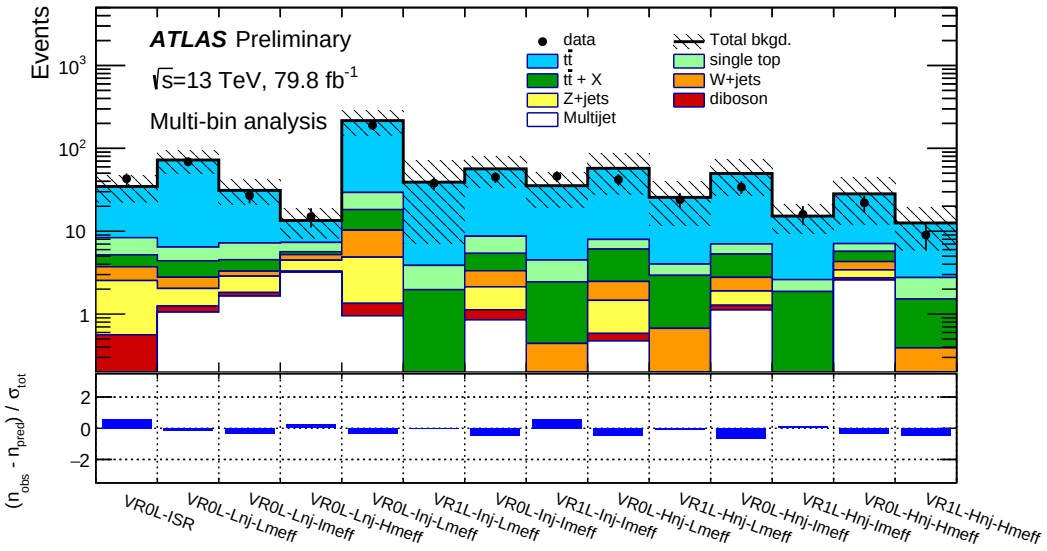

(b)

Figure 7: Results of the background-only fit extrapolated to the VRs for (a) the cut-and-count and (b) the multi-bin analyses. The data in the VRs are not included in the fit. The upper panel shows the observed number of events and the predicted background yield. All uncertainties defined in Section 7 are included in the uncertainty band. The background category $t\bar{t} + X$ includes $t\bar{t}W/Z$, $t\bar{t}H$ and $t\bar{t}t\bar{t}$ events. The lower panel shows the pulls in each VR.

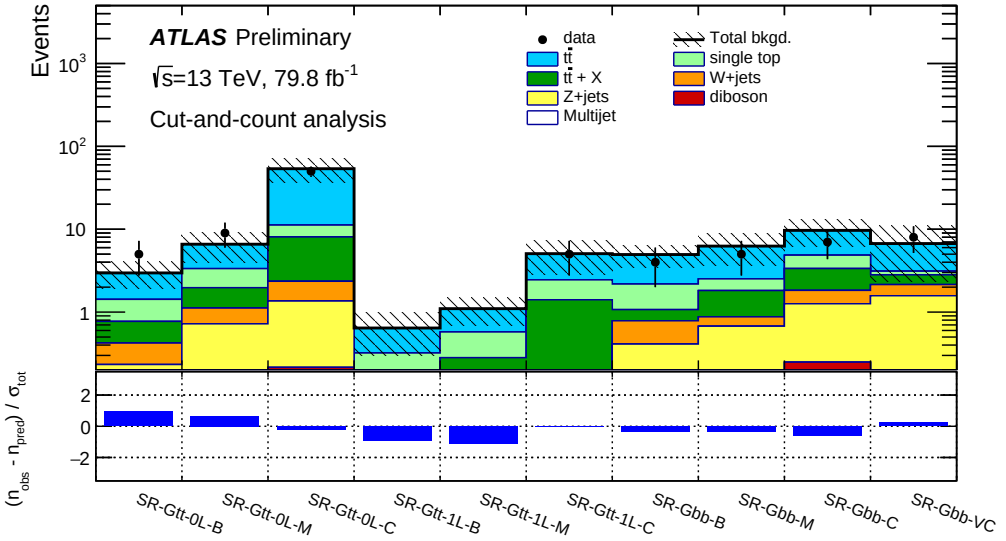

(a)

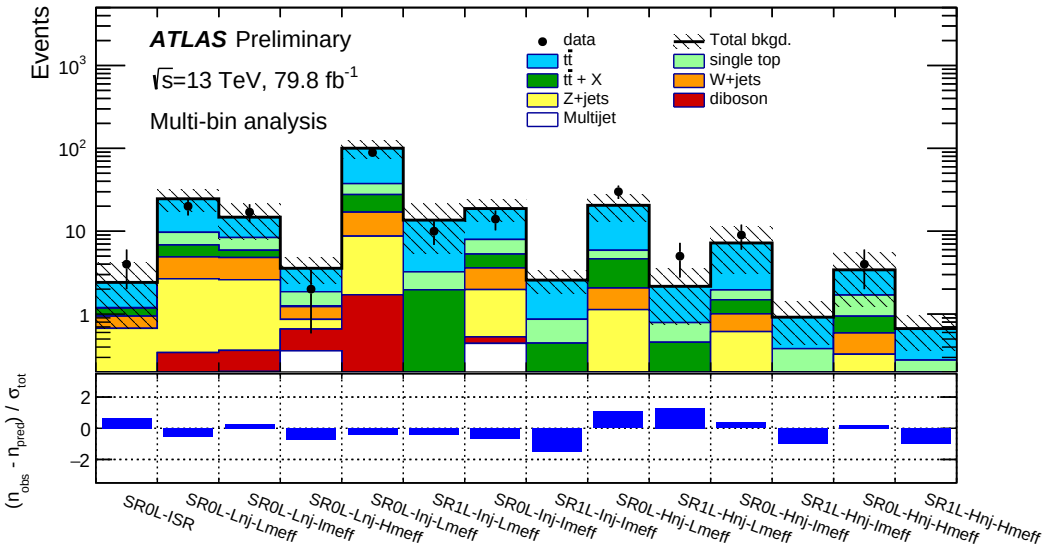

(b)

Figure 8: Results of the background-only fit extrapolated to the SRs for (a) the cut-and-count and (b) the multi-bin analyses. The data in the SRs are not included in the fit. The upper panel shows the observed number of events and the predicted background yield. All uncertainties defined in Section 7 are included in the uncertainty band. The background category $t\bar{t} + X$ includes $t\bar{t}W/Z$, $t\bar{t}H$ and $t\bar{t}t\bar{t}$ events. The lower panel shows the pull in each SR.

Table 5: Results of the background-only fit extrapolated to the Gtt 1-lepton, Gtt 0-lepton and Gbb SRs in the cut-and-count analysis, for the total background prediction and breakdown of the main background sources. The uncertainties shown include all systematic uncertainties. The data in the SRs are not included in the fit. The background category $t\bar{t}+X$ includes $t\bar{t}W/Z$, $t\bar{t}H$ and $t\bar{t}t\bar{t}$ events. The row "MC-only background" provides the total background prediction when the $t\bar{t}$ normalisation is obtained from a theoretical calculation [36]. Yields are obtained for large Δm ("B"), moderate Δm ("M"), small Δm ("C") and very small Δm ("VC") scenarios.

	SR-Gtt-1L		
Targeted kinematics	B	M	C
Observed events	0	0	5
Fitted background	0.64 ± 0.34	1.1 ± 0.4	5.1 ± 2.2
$t\bar{t}$	0.32 ± 0.23	0.52 ± 0.30	2.6 ± 1.7
Single-top	0.17 ± 0.22	0.29 ± 0.19	1.0 ± 1.0
$t\bar{t}+X$	0.15 ± 0.09	0.27 ± 0.15	1.4 ± 0.7
Z+jets	< 0.01	< 0.01	0.0018 ± 0.0015
W+jets	< 0.01	0.009 ± 0.031	0.007 ± 0.008
Diboson	< 0.01	< 0.01	< 0.01
MC-only background	0.8	1.1	5.3

	SR-Gtt-0L		
Targeted kinematics	B	M	C
Observed events	5	9	50
Fitted background	3.0 ± 1.1	6.6 ± 2.6	54 ± 17
$t\bar{t}$	1.5 ± 0.7	3.2 ± 1.8	42 ± 16
Single-top	0.7 ± 0.6	1.4 ± 0.7	3.2 ± 3.4
$t\bar{t}+X$	0.35 ± 0.19	0.9 ± 0.4	5.7 ± 3.1
Z+jets	0.2 ± 0.5	0.6 ± 1.7	1.1 ± 2.9
W+jets	0.19 ± 0.17	0.4 ± 0.4	1.0 ± 1.0
Diboson	< 0.01	0.06 ± 0.04	0.19 ± 0.13
Multijet	0.04 ± 0.04	0.029 ± 0.029	0.030 ± 0.030
MC-only background	3.3	7.2	52

	SR-Gbb			
Targeted kinematics	B	M	C	VC
Observed events	4	5	7	8
Fitted background	4.9 ± 1.5	6.3 ± 2.6	9.7 ± 3.5	7 ± 4
$t\bar{t}$	2.8 ± 0.9	3.7 ± 2.1	4.8 ± 1.4	3.6 ± 2.2
Single-top	1.1 ± 0.7	0.7 ± 0.4	1.5 ± 1.6	0.30 ± 0.26
$t\bar{t}+X$	0.29 ± 0.17	0.9 ± 0.5	1.5 ± 0.8	0.67 ± 0.35
Z+jets	0.3 ± 0.8	0.5 ± 1.3	1.0 ± 2.6	1 ± 4
W+jets	0.4 ± 0.4	0.20 ± 0.23	0.6 ± 0.5	0.6 ± 0.5
Diboson	0.03 ± 0.14	0.19 ± 0.24	0.25 ± 0.19	0.16 ± 0.11
Multijet	0.08 ± 0.08	< 0.01	< 0.01	< 0.01
MC-only background	4.5	7.0	9.0	7

9 Interpretation

In the absence of any significant excess over the expected background from SM processes, the data are used to derive one-sided upper limits at 95% confidence level (CL). Two levels of interpretation are provided in this note: model-independent exclusion limits and model-dependent exclusion limits set on the Gbb, Gtt and gluino variable branching ratio models.

9.1 Model-independent exclusion limits

Model-independent limits on the number of beyond-the-SM (BSM) events for each SR are derived with pseudoexperiments using the CL_s prescription [71], neglecting a possible signal contamination in the CR and following the procedure detailed in Ref. [17]. Only the single-bin regions from the cut-and-count analysis are used for this purpose, to aid in the reintepretation of these limits (see Table 6).

9.2 Model-dependent exclusion limits

The results are used to place exclusion limits on various signal models. The results are obtained using the CL_s prescription in the asymptotic approximation [69]. The signal contamination in the CRs and the experimental systematic uncertainties in the signal are taken into account for this calculation. All the regions of the multi-bin analysis are statistically combined to set model-dependent upper limits on the Gbb, Gtt and variable branching ratio models.

Table 6: The p_0-values and Z (the number of equivalent Gaussian standard deviations), the 95% CL upper limits on the visible cross-section (σ^{95}_{vis}), and the observed and expected 95% CL upper limits on the number of BSM events (S^{95}_{obs} and S^{95}_{exp}). The maximum allowed p_0-value is truncated at 0.5.

Signal channel	p_0 (Z)	σ^{95}_{vis} [fb]	S^{95}_{obs}	S^{95}_{exp}
SR-Gtt-1L-B	0.50 (0.00)	0.04	3.1	$3.1^{+1.1}_{-0.0}$
SR-Gtt-1L-M	0.50 (0.00)	0.04	3.0	$3.6^{+1.4}_{-0.6}$
SR-Gtt-1L-C	0.50 (0.00)	0.09	7.1	$7.1^{+2.6}_{-1.9}$
SR-Gtt-0L-B	0.16 (0.99)	0.10	7.7	$5.4^{+2.3}_{-1.2}$
SR-Gtt-0L-M	0.25 (0.67)	0.13	10.6	$8.4^{+3.1}_{-2.0}$
SR-Gtt-0L-C	0.50 (0.00)	0.38	30.4	$31.5^{+9.4}_{-7.7}$
SR-Gbb-B	0.50 (0.00)	0.07	5.8	$6.2^{+2.4}_{-1.5}$
SR-Gbb-M	0.50 (0.00)	0.09	6.9	$7.4^{+2.8}_{-1.7}$
SR-Gbb-C	0.50 (0.00)	0.10	7.7	$8.8^{+3.2}_{-2.2}$
SR-Gbb-VC	0.38 (0.31)	0.15	11.8	$10.6^{+3.3}_{-2.1}$

The 95% CL observed and expected exclusion limits for the Gtt and Gbb models are shown in the LSP and gluino mass plane in Figures 9(a) and 9(b), respectively. The $\pm 1\sigma^{\text{SUSY}}_{\text{theory}}$ lines around the observed limits are obtained by changing the SUSY production cross-section by one standard deviation ($\pm 1\sigma$), as described in Section 3. The yellow band around the expected limit shows the $\pm 1\sigma$ uncertainty, including all statistical and systematic uncertainties except the theoretical uncertainties in the SUSY cross-section. Compared to the previous results [17], the gluino mass sensitivities of the current search (assuming massless LSPs) have improved by 280 GeV and 270 GeV for the Gbb and Gtt models, respectively. Gluinos with masses below 2.2 TeV are excluded at 95% CL for neutralino masses lower than 800 GeV in the Gtt and Gbb models. The best exclusion limits on the LSP mass are approximately 1.3 and 1.2 TeV, reached for a gluino mass of approximately 1.8 and 2.1 TeV for Gbb and Gtt models, respectively.

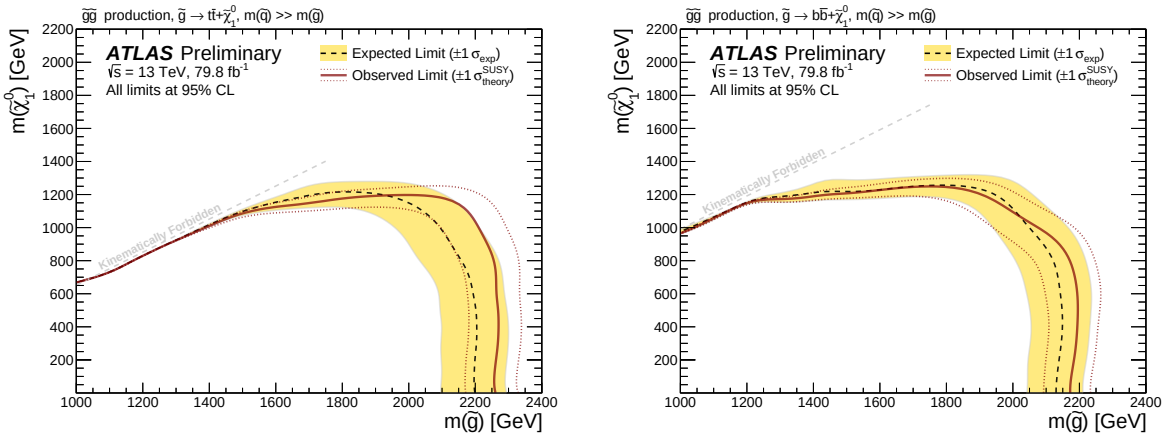

(a) (b)

Figure 9: Exclusion limits in the $\tilde{\chi}^0_1$ and $\tilde{g}$ mass plane for the (a) Gtt and (b) Gbb models obtained in the context of the multi-bin analysis. The dashed and solid bold lines show the 95% CL expected and observed limits, respectively. The shaded bands around the expected limits show the impact of the experimental and background uncertainties. The dotted lines show the impact on the observed limit of the variation of the nominal signal cross-section by $\pm 1\sigma$ of its theoretical uncertainty.

Figure 10 shows the expected (10(a)) and observed (10(b)) 95% CL exclusion limits as a function of the gluino branching ratio to Gbb (vertical) and Gtt (horizontal) models. Gluinos not decaying to either the Gtt or Gbb mode are assumed to decay via Gtb instead, and $m(\tilde{\chi}^0_1)$ is fixed to 1 GeV. The exclusion reach is highest in the pure Gtt corner of the branching ratio space, and weakest in the pure Gtb corner. Similar results, with $m(\tilde{\chi}^0_1) = 600$ GeV and $m(\tilde{\chi}^0_1) = 1000$ GeV, are shown in Figures 11 and 12. As the mass of the $\tilde{\chi}^0_1$ increases, the sensitivity becomes weakest for mixed Gtb and Gbb models. The decreased sensitivity motivates future optimization for these mixed topologies.

Additionally, the 95% CL observed and expected exclusion limits as a function of $m(\tilde{t})$ for the Gtt model with an on-shell stop are shown in Figure 13. The $\tilde{g}$ and $\tilde{\chi}^0_1$ masses are fixed to 2.1 TeV and 600 GeV respectively. As can be observed in Figure 13, when the mass of the stop is far from $m(\tilde{g})$ and $m(\tilde{\chi}^0_1)$ (1.2 TeV $\lesssim m(\tilde{t}) \lesssim$ 1.7 TeV), the exclusion limit is similar to that of the off-shell result, but when $m(\tilde{t})$ is close to the $\tilde{g}$ mass (1.8 TeV $\lesssim m(\tilde{t})$) or $\tilde{\chi}^0_1$ mass ($m(\tilde{t}) \lesssim 1$ TeV), the limit degrades because one of the tops in the decay chain loses substantial energy.

Figure 14 shows the expected and observed the 95% CL cross-section upper limit for the Gtb model with

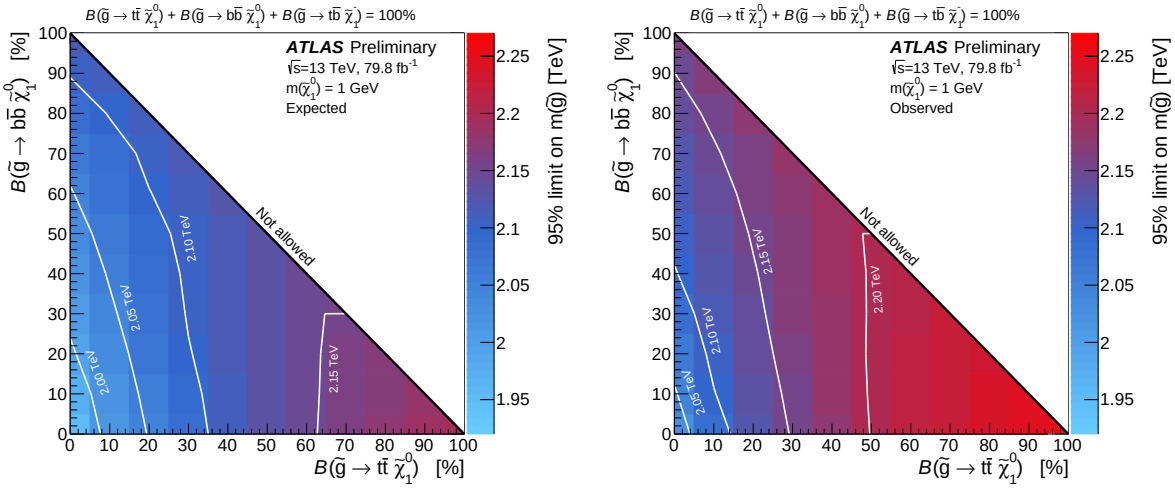

(a) (b)

Figure 10: The expected (a) and observed (b) 95% CL exclusion limits on the gluino mass as a function of the gluino branching ratio to Gbb (vertical) and Gtt (horizontal) models. Gluinos not decaying to either the Gtt or Gbb mode are assumed to decay via Gtb instead. In this figure $m(\tilde{\chi}_1^0)$ is fixed to 1 GeV. The z-axis indicates the maximum excluded gluino mass for each point in the branching ratio space. The white lines indicate contours at mass intervals of 50 GeV. The exclusion limits were derived using the multibin analysis.

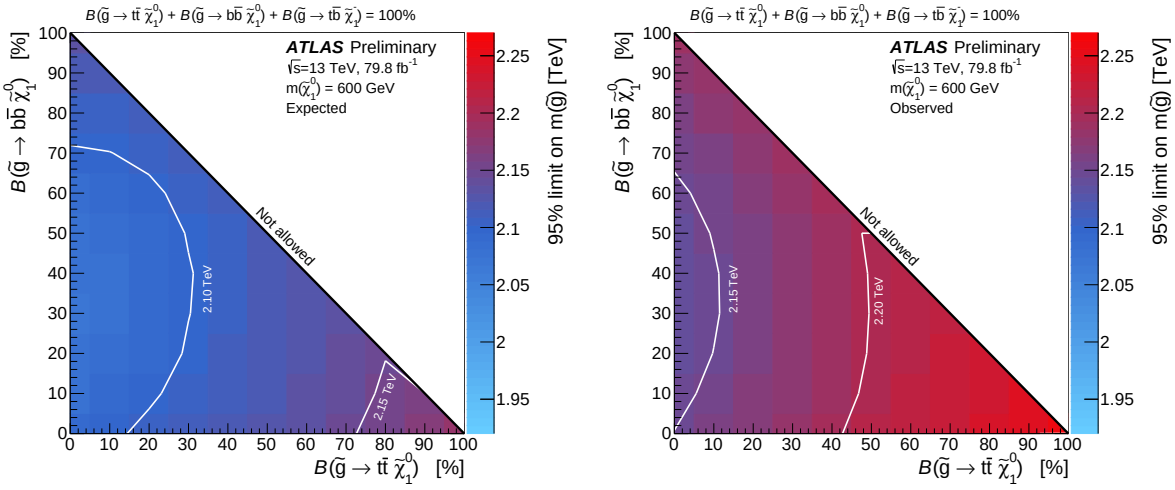

(a) (b)

Figure 11: The expected (a) and observed (b) 95% CL exclusion limits on the gluino mass as a function of the gluino branching ratio to Gbb (vertical) and Gtt (horizontal) models. Gluinos not decaying to either the Gtt or Gbb mode are assumed to decay via Gtb instead. In this figure $m(\tilde{\chi}_1^0)$ is fixed to 600 GeV. The z-axis indicates the maximum excluded gluino mass for each point in the branching ratio space. The white lines indicate contours at mass intervals of 50 GeV. The exclusion limits were derived using the multibin analysis.

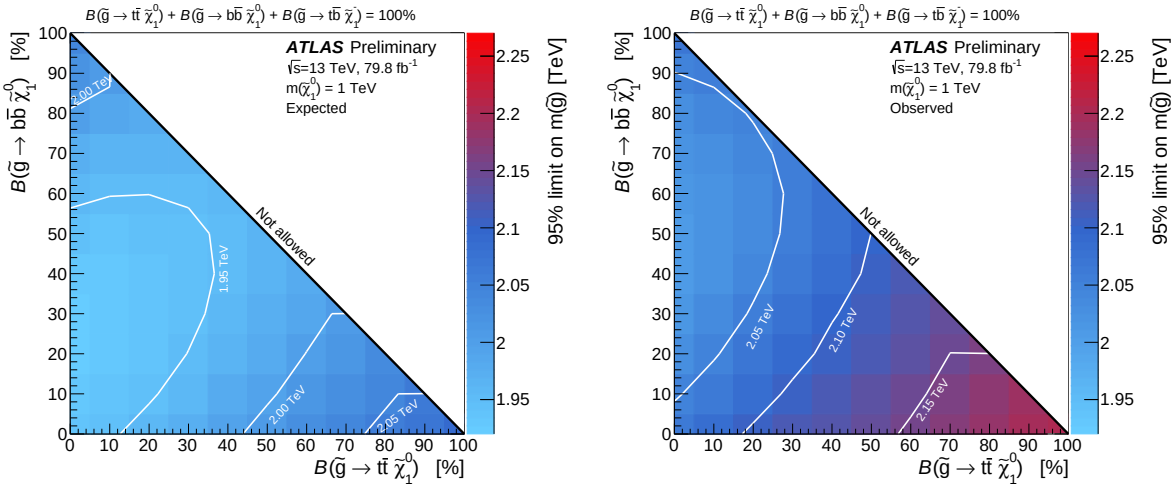

(a) (b)

Figure 12: The expected (a) and observed (b) 95% CL exclusion limits on the gluino mass as a function of the gluino branching ratio to Gbb (vertical) and Gtt (horizontal) models. Gluinos not decaying to either the Gtt or Gbb mode are assumed to decay via Gtb instead. In this figure $m(\tilde{\chi}_1^0)$ is fixed to 1000 GeV. The z-axis indicates the maximum excluded gluino mass for each point in the branching ratio space. The white lines indicate contours at mass intervals of 50 GeV. The exclusion limits were derived using the multibin analysis.

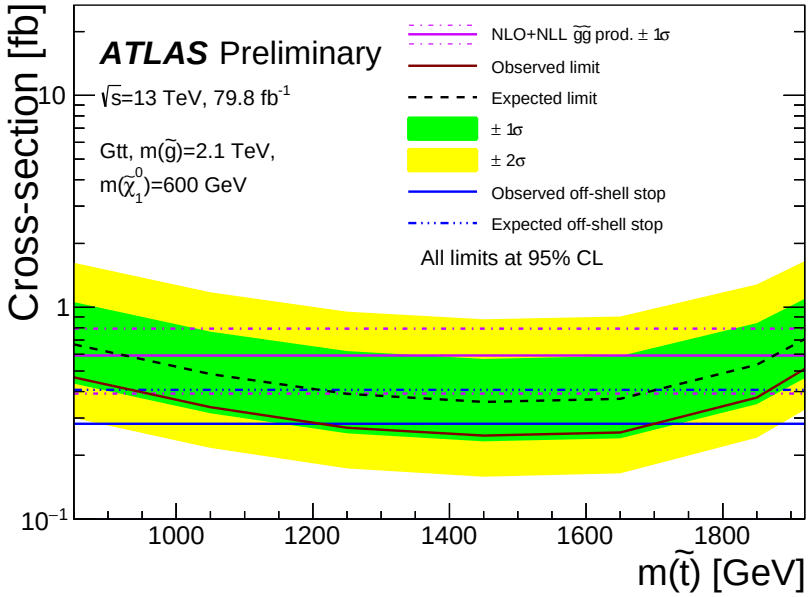

Figure 13: Exclusion limits as a function of $m(\tilde{t})$, in the Gtt model but with an on-shell stop, in the context of the multi-bin analysis. The $\tilde{g}$ and $\tilde{\chi}_1^0$ masses are fixed to 2.1 TeV and 600 GeV respectively. The dashed and solid bold lines show the 95% CL expected and observed limits, respectively. The solid red line indicates the theoretical cross-section for a 2.1 TeV gluino. The thin blue lines indicate the expected (dashed) and observed (solid) limits for the case of the off-shell stop, where $m(\tilde{t}) = 5$ TeV.

on-shell stop, sbottom and $\tilde{\chi}_1^{\pm}$, as a function of the stop mass. The $\tilde{g}$ and $\tilde{\chi}_1^0$ masses are fixed to 2.1 TeV and 600 GeV respectively, the $\tilde{\chi}_1^{\pm}$ mass is fixed to either 1.2 TeV (Figure 14(a)) or 180 GeV lower than the stop mass (14(b)), and the sbottom mass is fixed at the same value as $m(\tilde{t})$. In the range considered for the masses of stop and sbottom, the cross-section limit does not depend strongly on the stop and sbottom mass in the case of fixed $m(\tilde{\chi}_1^{\pm})$, while when an increase in stop mass corresponds also to an increase in $m(\tilde{\chi}_1^{\pm})$, the limit is weaker for higher values of $m(\tilde{t})$.

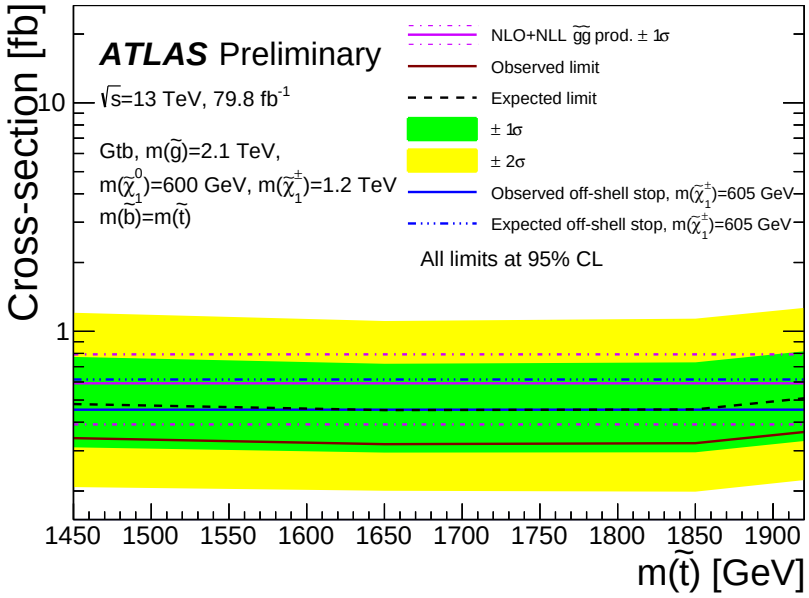

(a)

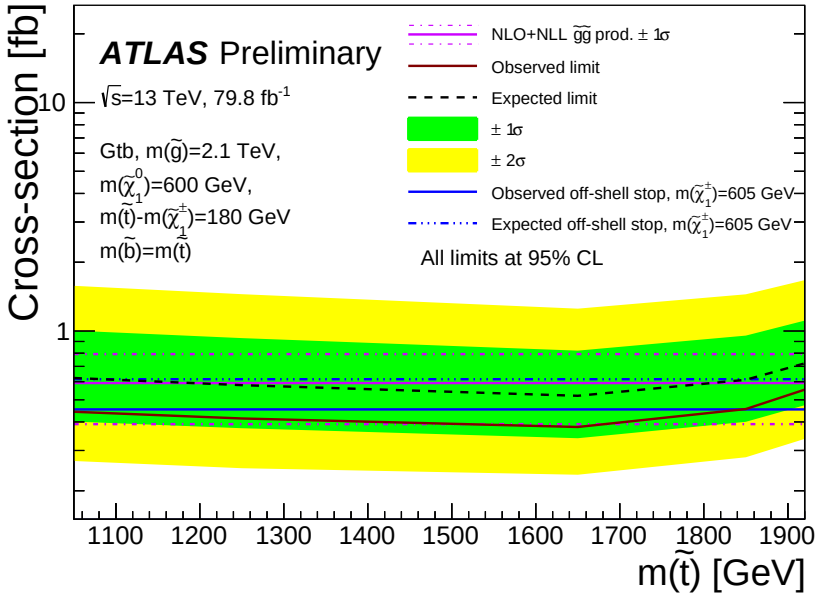

(b)

Figure 14: Exclusion limits as a function of $m(\tilde{t})$, in the Gtb model but with an on-shell stop and $\tilde{\chi}_1^{\pm}$, for $\tilde{\chi}_1^{\pm}$ mass fixed to 1.2 TeV (a) and 180 GeV lower than the stop mass (b), in the context of the multi-bin analysis. The $\tilde{g}$ and $\tilde{\chi}_1^0$ masses are fixed to 2.1 TeV and 600 GeV respectively. The dashed and solid bold lines show the 95% CL expected and observed limits, respectively. The solid red line indicates the theoretical cross-section for a 2.1 TeV gluino. The thin blue lines indicate the expected (dashed) and observed (solid) limits for the case of the off-shell stop, where $m(\tilde{t}) = 5$ TeV, and $m(\tilde{\chi}_1^{\pm}) = 605$ GeV.

10 Conclusion

A search for pair-produced gluinos decaying via bottom or top squarks is presented. LHC proton–proton collision data from the full 2015–2017 data-taking periods are analysed, corresponding to an integrated luminosity of 79.8 fb^{-1} collected at $\sqrt{s}$ = 13 TeV by the ATLAS detector. The search uses multiple signal regions designed for different scenarios of gluino and LSP masses. The signal regions require several high-p_{T} jets, of which at least three must be b-tagged, large $E_{\mathrm{T}}^{\mathrm{miss}}$ and either zero or at least one charged lepton. Two strategies are employed: one in which the signal regions are optimised for discovery, and another one in which several non-overlapping signal regions are fitted simultaneously to achieve optimal exclusion limits for benchmark signals. For all signal regions, the background is generally dominated by $t\bar{t}$+jets, which is normalised in dedicated control regions. No significant excess is found above the predicted background in any of the signal regions. Model-independent limits are set on the visible cross-section for new physics processes. Exclusion limits are set on gluino and LSP masses in two simplified models where the gluino decays exclusively as $\tilde{g} \to b\bar{b}\tilde{\chi}_1^0$ or $\tilde{g} \to t\bar{t}\tilde{\chi}_1^0$. For LSP masses below approximately 800 GeV, gluino masses of less than 2.2 TeV are excluded at the 95% CL for the $\tilde{g} \to t\bar{t}\tilde{\chi}_1^0$ and $\tilde{g} \to b\bar{b}\tilde{\chi}_1^0$ models. The results are also interpreted in a model with variable gluino branching ratios to $\tilde{g} \to b\bar{b}\tilde{\chi}_1^0$, $\tilde{g} \to t\bar{b}\tilde{\chi}_1^-$ and $\tilde{g} \to t\bar{t}\tilde{\chi}_1^0$. For example, signal models with $B(\tilde{g} \to t\bar{b}\tilde{\chi}_1^-)$ near 100% and $m(\tilde{\chi}_1^0)$ = 1 GeV are excluded at the 95% CL for $m(\tilde{g}) \lesssim 2$ TeV.

Appendix

The raw number of MC signal events after each selection is reported in the Tables below for all cut-and-count regions. Representative signal models are considered for each region.

Gbb-0L-M Gbb, $m_{\tilde{g}}$ = 1900 GeV, $m_{\tilde{\chi}_1^0}$ = 1400 GeV	
Cut stage	Num. events
Total	126.5
Trigger	104.0
0L Preselection	69.4
$E_{\mathrm{T}}^{\mathrm{miss}} \geq 450$ GeV	28.8
$N_{b\text{-jets}} \geq 4$	7.2
$m_{\mathrm{T,min}}^{b\text{-jets}} \geq 155$ GeV	6.7

Table 7: Example cutflow for Gbb-0L-M.

Gbb-0L-C Gbb, $m_{\tilde{g}}$ = 1900 GeV, $m_{\tilde{\chi}_1^0}$ = 1400 GeV	
Cut stage	Num. events
Total	126.5
Trigger	104.0
0L Preselection	69.4
$E_{\mathrm{T}}^{\mathrm{miss}} \geq 450$ GeV	28.8
$N_{b\text{-jets}} \geq 4$	7.2
$m_{\mathrm{T,min}}^{b\text{-jets}} \geq 90$ GeV	7.1
$m_{\mathrm{eff}} \geq 1600$ GeV	2.8

Table 8: Example cutflow for Gbb-0L-C.

Gbb-0L-B Gbb, $m_{\tilde{g}} = 1900$ GeV, $m_{\tilde{\chi}_1^0} = 1400$ GeV	
Cut stage	Num. events
Total	126.5
Trigger	104.0
0L Preselection	69.4
$E_{\mathrm{T}}^{\mathrm{miss}} \geq 400$ GeV	36.8
$N_{b\text{-jets}} \geq 3$	25.3
$m_{\mathrm{eff}} \geq 2800$ GeV	0.5

Table 9: Example cutflow for Gbb-0L-B.

Gbb-0L-VC Gbb, $m_{\tilde{g}} = 1900$ GeV, $m_{\tilde{\chi}_1^0} = 1400$ GeV	
Cut stage	Num. events
Total	126.5
Trigger	104.0
0L Preselection	69.4
$E_{\mathrm{T}}^{\mathrm{miss}} \geq 600$ GeV	11.6
$N_{b\text{-jets}} \geq 4$	2.7
$m_{\mathrm{T,min}}^{b\text{-jets}} \geq 100$ GeV	2.6
$m_{\mathrm{eff}} \geq 1600$ GeV	1.3
$p_{\mathrm{T}}^{\mathrm{j}_1} > 400$ GeV	0.6
$\mathrm{j}_1 \neq b$	0.5

Table 10: Example cutflow for Gbb-0L-VC.

Gtt-1L-B Gtt, $m_{\tilde{g}} = 1900$ GeV, $m_{\tilde{\chi}_1^0} = 1$ GeV	
Cut stage	Num. events
Total	131.4
Trigger	121.5
1L Preselection	50.5
$E_{\mathrm{T}}^{\mathrm{miss}} \geq 500$ GeV	33.6
$m_{\mathrm{T}} > 150$ GeV	28.3
$N_{\mathrm{jet}} \geq 5$	27.6
$N_{b\text{-jets}} \geq 3$	16.8
$m_{\mathrm{T,min}}^{b\text{-jets}} \geq 120$ GeV	13.6
$M_J^{\Sigma} \geq 200$ GeV	11.8
$m_{\mathrm{eff}} \geq 2200$ GeV	10.5

Table 11: Example cutflow for Gtt-1L-B.

Gtt-1L-C Gtt, $m_{\tilde{g}} = 1900$ GeV, $m_{\tilde{\chi}_1^0} = 1$ GeV	
Cut stage	Num. events
Total	131.4
Trigger	121.5
1L Preselection	50.5
$E_{\mathrm{T}}^{\mathrm{miss}} \geq 350$ GeV	43.4
$m_{\mathrm{T}} > 150$ GeV	36.0
$N_{\mathrm{jet}} \geq 7$	26.2
$N_{b\text{-jets}} \geq 3$	17.0
$m_{\mathrm{T,min}}^{b\text{-jets}} \geq 160$ GeV	12.3
$m_{\mathrm{eff}} \geq 1000$ GeV	12.3

Table 12: Example cutflow for Gtt-1L-C.

Gtt-0L-M Gtt, $m_{\tilde{g}} = 1900$ GeV, $m_{\tilde{\chi}_1^0} = 1$ GeV	
Cut stage	Num. events
Total	131.4
Trigger	121.5
0L Preselection	36.5
$E_{\mathrm{T}}^{\mathrm{miss}} \geq 500$ GeV	26.4
$N_{\mathrm{jet}} \geq 7$	23.8
$N_{b\text{-jets}} \geq 3$	15.6
$m_{\mathrm{T,min}}^{b\text{-jets}} \geq 120$ GeV	13.7
$M_J^{\Sigma} \geq 200$ GeV	13.3
$m_{\mathrm{eff}} \geq 1800$ GeV	13.1

Table 13: Example cutflow for Gtt-0L-M.

Gtt-0L-C Gtt, $m_{\tilde{g}} = 1900$ GeV, $m_{\tilde{\chi}_1^0} = 1$ GeV	
Cut stage	Num. events
Total	131.4
Trigger	121.5
0L Preselection	36.5
$N_{\mathrm{jet}} \geq 8$	28.2
$N_{b\text{-jets}} \geq 4$	8.2
$m_{\mathrm{T,min}}^{b\text{-jets}} \geq 120$ GeV	7.3
$M_J^{\Sigma} \geq 100$ GeV	7.3
$m_{\mathrm{eff}} \geq 1000$ GeV	7.3

Table 14: Example cutflow for Gtt-0L-C.

Gtt-0L-B Gtt, $m_{\tilde{g}} = 1900$ GeV, $m_{\tilde{\chi}_1^0} = 1$ GeV	
Cut stage	Num. events
Total	131.4
Trigger	121.5
0L Preselection	36.5
$E_{\mathrm{T}}^{\mathrm{miss}} \geq 350$ GeV	32.3
$N_{\mathrm{jet}} \geq 7$	29.2
$N_{b\text{-jets}} \geq 3$	19.2
$m_{\mathrm{T,min}}^{b\text{-jets}} \geq 60$ GeV	17.9
$M_J^{\Sigma} \geq 300$ GeV	14.7
$m_{\mathrm{eff}} \geq 2600$ GeV	10.8

Table 15: Example cutflow for Gtt-0L-B.

Gtt-1L-M Gtt, $m_{\tilde{g}} = 1900$ GeV, $m_{\tilde{\chi}_1^0} = 1$ GeV	
Cut stage	Num. events
Total	131.4
Trigger	121.5
1L Preselection	50.5
$E_{\mathrm{T}}^{\mathrm{miss}} \geq 450$ GeV	37.1
$m_{\mathrm{T}} > 150$ GeV	31.0
$N_{\mathrm{jet}} \geq 6$	27.6
$N_{b\text{-jets}} \geq 3$	17.3
$m_{\mathrm{T,min}}^{b\text{-jets}} \geq 160$ GeV	12.8
$M_J^{\Sigma} \geq 200$ GeV	11.3
$m_{\mathrm{eff}} \geq 1800$ GeV	11.2

Table 16: Example cutflow for Gtt-1L-M.

References

[1] Y. A. Golfand and E. P. Likhtman, *Extension of the Algebra of Poincare Group Generators and Violation of p Invariance*, JETP Lett. **13** (1971) 323, [Pisma Zh. Eksp. Teor. Fiz. **13** (1971) 452].

[2] D. V. Volkov and V. P. Akulov, *Is the Neutrino a Goldstone Particle?*, Phys. Lett. B **46** (1973) 109.

[3] J. Wess and B. Zumino, *Supergauge Transformations in Four-Dimensions*, Nucl. Phys. B **70** (1974) 39.

[4] J. Wess and B. Zumino, *Supergauge Invariant Extension of Quantum Electrodynamics*, Nucl. Phys. B **78** (1974) 1.

[5] S. Ferrara and B. Zumino, *Supergauge Invariant Yang-Mills Theories*, Nucl. Phys. B **79** (1974) 413.

[6] A. Salam and J. A. Strathdee, *Supersymmetry and Nonabelian Gauges*, Phys. Lett. B **51** (1974) 353.

[7] G. R. Farrar and P. Fayet, *Phenomenology of the Production, Decay, and Detection of New Hadronic States Associated with Supersymmetry*, Phys. Lett. B **76** (1978) 575.

[8] N. Sakai, *Naturalness in Supersymmetric Guts*, Z. Phys. C **11** (1981) 153.

[9] S. Dimopoulos, S. Raby and F. Wilczek, *Supersymmetry and the Scale of Unification*, Phys. Rev. D **24** (1981) 1681.

[10] L. E. Ibanez and G. G. Ross, *Low-Energy Predictions in Supersymmetric Grand Unified Theories*, Phys. Lett. B **105** (1981) 439.

[11] S. Dimopoulos and H. Georgi, *Softly Broken Supersymmetry and SU(5)*, Nucl. Phys. B **193** (1981) 150.

[12] M. Papucci, J. T. Ruderman and A. Weiler, *Natural SUSY Endures*, JHEP **09** (2012) 035, arXiv: 1110.6926 [hep-ph].

[13] R. Barbieri and G. F. Giudice, *Upper Bounds on Supersymmetric Particle Masses*, Nucl. Phys. B **306** (1988) 63.

[14] J. Alwall, M.-P. Le, M. Lisanti and J. G. Wacker, *Searching for Directly Decaying Gluinos at the Tevatron*, Phys. Lett. B **666** (2008) 34, arXiv: 0803.0019 [hep-ph].

[15] J. Alwall, P. Schuster and N. Toro, *Simplified Models for a First Characterization of New Physics at the LHC*, Phys. Rev. D **79** (2009) 075020, arXiv: 0810.3921 [hep-ph].

[16] D. Alves et al., *Simplified Models for LHC New Physics Searches*, J. Phys. G **39** (2012) 105005, arXiv: 1105.2838 [hep-ph].

[17] ATLAS Collaboration, *Search for Supersymmetry in final states with missing transverse momentum and multiple b-jets in proton–proton collisions at* $\sqrt{s} = 13$ *TeV with the ATLAS detector*, JHEP **06** (2017) 107, arXiv: 1711.01901 [hep-ex].

[18] ATLAS Collaboration, *Search for supersymmetry at* $\sqrt{s} = 13$ *TeV in final states with jets and two same-sign leptons or three leptons with the ATLAS detector*, Eur. Phys. J. C **76** (2016) 259, arXiv: 1602.09058 [hep-ex].

[19] ATLAS Collaboration, *Search for supersymmetry in final states with two same-sign or three leptons and jets using 36* fb^{-1} *of* $\sqrt{s} = 13$ *TeV pp collision data with the ATLAS detector*, JHEP **09** (2017) 084, arXiv: 1706.03731 [hep-ex].

[20] CMS Collaboration, *Search for physics beyond the standard model in events with two leptons of same sign, missing transverse momentum, and jets in proton–proton collisions at* $\sqrt{s} = 13$ *TeV*, Eur. Phys. J. C **77** (2017) 578, arXiv: 1704.07323 [hep-ex].

[21] CMS Collaboration, *Search for supersymmetry in pp collisions at $\sqrt{s}$ = 13 TeV in the single-lepton final state using the sum of masses of large-radius jets*, Phys. Rev. Lett. **119** (2017) 151802, arXiv: 1705.04673 [hep-ex].

[22] CMS Collaboration, *Search for supersymmetry in multijet events with missing transverse momentum in proton–proton collisions at* 13 *TeV*, Phys. Rev. D **96** (2017) 032003, arXiv: 1704.07781 [hep-ex].

[23] CMS Collaboration, *Search for new phenomena with the M_{T2} variable in the all-hadronic final state produced in proton–proton collisions at $\sqrt{s}$ = 13 TeV*, Eur. Phys. J. C **77** (2017) 710, arXiv: 1705.04650 [hep-ex].

[24] ATLAS Collaboration, *The ATLAS Experiment at the CERN Large Hadron Collider*, JINST **3** (2008) S08003.

[25] ATLAS Collaboration, *ATLAS Insertable B-Layer Technical Design Report*, ATLAS-TDR-19, 2010, URL: https://cds.cern.ch/record/1291633, ATLAS Insertable B-Layer Technical Design Report Addendum, ATLAS-TDR-19-ADD-1, 2012, URL: https://cds.cern.ch/record/1451888.

[26] ATLAS Collaboration, *Performance of the ATLAS Trigger System in 2015*, Eur. Phys. J. C **77** (2017) 317, arXiv: 1611.09661 [hep-ex].

[27] S. Alioli, P. Nason, C. Oleari and E. Re, *A general framework for implementing NLO calculations in shower Monte Carlo programs: the POWHEG BOX*, JHEP **06** (2010) 043, arXiv: 1002.2581 [hep-ph].

[28] R. D. Ball et al., *Parton distributions for the LHC Run II*, JHEP **04** (2015) 040, arXiv: 1410.8849 [hep-ph].

[29] T. Sjöstrand, S. Mrenna and P. Z. Skands, *A Brief Introduction to PYTHIA 8.1*, Comput. Phys. Commun. **178** (2008) 852, arXiv: 0710.3820 [hep-ph].

[30] W. Beenakker, R. Hopker, M. Spira and P. Zerwas, *Squark and gluino production at hadron colliders*, Nucl. Phys. B **492** (1997) 51, arXiv: hep-ph/9610490.

[31] A. Kulesza and L. Motyka, *Threshold resummation for squark-antisquark and gluino-pair production at the LHC*, Phys. Rev. Lett. **102** (2009) 111802, arXiv: 0807.2405 [hep-ph].

[32] A. Kulesza and L. Motyka, *Soft gluon resummation for the production of gluino-gluino and squark-antisquark pairs at the LHC*, Phys. Rev. D **80** (2009) 095004, arXiv: 0905.4749 [hep-ph].

[33] W. Beenakker et al., *Soft-gluon resummation for squark and gluino hadroproduction*, JHEP **12** (2009) 041, arXiv: 0909.4418 [hep-ph].

[34] W. Beenakker et al., *Squark and gluino hadroproduction*, Int. J. Mod. Phys. A **26** (2011) 2637, arXiv: 1105.1110 [hep-ph].

[35] C. Borschensky et al., *Squark and gluino production cross sections in pp collisions at $\sqrt{s}$ = 13, 14, 33 and 100 TeV*, Eur. Phys. J. C **74** (2014) 3174, arXiv: 1407.5066 [hep-ph].

[36] M. Czakon and A. Mitov, *Top++: A Program for the Calculation of the Top-Pair Cross-Section at Hadron Colliders*, Comput. Phys. Commun. **185** (2014) 2930, arXiv: 1112.5675 [hep-ph].

[37] N. Kidonakis, *Next-to-next-to-leading-order collinear and soft gluon corrections for t-channel single top quark production*, Phys. Rev. D **83** (2011) 091503, arXiv: 1103.2792 [hep-ph].

[38] N. Kidonakis, *Two-loop soft anomalous dimensions for single top quark associated production with a W^- or H^-*, Phys. Rev. D **82** (2010) 054018, arXiv: 1005.4451 [hep-ph].

[39] N. Kidonakis, *NNLL resummation for s-channel single top quark production*, Phys. Rev. D **81** (2010) 054028, arXiv: 1001.5034 [hep-ph].

[40] J. Alwall et al., *The automated computation of tree-level and next-to-leading order differential cross sections, and their matching to parton shower simulations*, JHEP **07** (2014) 079, arXiv: 1405.0301 [hep-ph].

[41] J. R. Andersen et al., *Handbook of LHC Higgs Cross Sections: 3. Higgs Properties*, CERN-2013-004, 10.5170/CERN-2013-004, 2013, arXiv: 1307.1347 [hep-ph].

[42] T. Gleisberg et al., *Event generation with SHERPA 1.1*, JHEP **02** (2009) 007, arXiv: 0811.4622 [hep-ph].

[43] S. Höche, F. Krauss, M. Schönherr and F. Siegert, *QCD matrix elements + parton showers: The NLO case*, JHEP **04** (2013) 027, arXiv: 1207.5030 [hep-ph].

[44] S. Catani, L. Cieri, G. Ferrera, D. de Florian and M. Grazzini, *Vector boson production at hadron colliders: a fully exclusive QCD calculation at NNLO*, Phys. Rev. Lett. **103** (2009) 082001, arXiv: 0903.2120 [hep-ph].

[45] ATLAS Collaboration, *Vertex Reconstruction Performance of the ATLAS Detector at* $\sqrt{s} = 13$ *TeV*, ATL-PHYS-PUB-2015-026, 2015, URL: https://cds.cern.ch/record/2037717.

[46] ATLAS Collaboration, *Electron and photon energy calibration with the ATLAS detector using LHC Run 1 data*, Eur. Phys. J. C **74** (2014) 3071, arXiv: 1407.5063 [hep-ex].

[47] ATLAS Collaboration, *Electron efficiency measurements with the ATLAS detector using the 2015 LHC proton–proton collision data*, ATLAS-CONF-2016-024, 2016, URL: https://cds.cern.ch/record/2157687.

[48] ATLAS Collaboration, *Muon reconstruction performance of the ATLAS detector in proton–proton collision data at* $\sqrt{s} = 13$ *TeV*, Eur. Phys. J. C **76** (2016) 292, arXiv: 1603.05598 [hep-ex].

[49] ATLAS Collaboration, *Topological cell clustering in the ATLAS calorimeters and its performance in LHC Run 1*, Eur. Phys. J. C **77** (2017) 490, arXiv: 1603.02934 [hep-ex].

[50] M. Cacciari, G. P. Salam and G. Soyez, *The anti-*k_t *jet clustering algorithm*, JHEP **04** (2008) 063, arXiv: 0802.1189 [hep-ph].

[51] M. Cacciari, G. P. Salam and G. Soyez, *FastJet User Manual*, Eur. Phys. J. C **72** (2012) 1896, arXiv: 1111.6097 [hep-ph].

[52] ATLAS Collaboration, *Jet energy scale measurements and their systematic uncertainties in proton–proton collisions at* $\sqrt{s} = 13$ *TeV with the ATLAS detector*, Phys. Rev. D **96** (2017) 072002, arXiv: 1703.09665 [hep-ex].

[53] ATLAS Collaboration, *Selection of jets produced in* 13 *TeV proton–proton collisions with the ATLAS detector*, ATLAS-CONF-2015-029, 2015, URL: https://cds.cern.ch/record/2037702.

[54] ATLAS Collaboration, *Performance of pile-up mitigation techniques for jets in pp collisions at* $\sqrt{s} = 8$ *TeV using the ATLAS detector*, Eur. Phys. J. C **76** (2016) 581, arXiv: 1510.03823 [hep-ex].

[55] ATLAS Collaboration, *Performance of b-jet identification in the ATLAS experiment*, JINST **11** (2016) P04008, arXiv: 1512.01094 [hep-ex].

[56] ATLAS Collaboration, *Optimisation of the ATLAS b-tagging performance for the 2016 LHC Run*, ATL-PHYS-PUB-2016-012, URL: https://cds.cern.ch/record/2160731.

[57] B. Nachman, P. Nef, A. Schwartzman, M. Swiatlowski and C. Wanotayaroj, *Jets from Jets: Re-clustering as a tool for large radius jet reconstruction and grooming at the LHC*, JHEP **02** (2015) 075, arXiv: 1407.2922 [hep-ph].

[58] D. Krohn, J. Thaler and L.-T. Wang, *Jet Trimming*, JHEP **02** (2010) 084, arXiv: 0912.1342 [hep-ph].

[59] ATLAS Collaboration, *Performance of jet substructure techniques for large-R jets in proton–proton collisions at* $\sqrt{s} = 7$ *TeV using the ATLAS detector*, JHEP **09** (2013) 076, arXiv: 1306.4945 [hep-ex].

[60] ATLAS Collaboration, *Performance of Top Quark and W Boson Tagging in Run 2 with ATLAS*, ATLAS-CONF-2017-064, 2017, URL: https://cds.cern.ch/record/2281054.

[61] ATLAS Collaboration, *Performance of missing transverse momentum reconstruction with the ATLAS detector in the first proton–proton collisions at* $\sqrt{s} = 13$ *TeV*, ATL-PHYS-PUB-2015-027, 2015, URL: https://cds.cern.ch/record/2037904.

[62] ATLAS Collaboration, *Expected performance of missing transverse momentum reconstruction for the ATLAS detector at* $\sqrt{s} = 13$ *TeV*, ATL-PHYS-PUB-2015-023, 2015, URL: https://cds.cern.ch/record/2037700.

[63] ATLAS Collaboration, *Search for pair production of up-type vector-like quarks and for four-top-quark events in final states with multiple b-jets with the ATLAS detector*, JHEP **07** (2018) 089, arXiv: 1803.09678 [hep-ex].

[64] ATLAS Collaboration, *Luminosity determination in pp collisions at* $\sqrt{s} = 8$ *TeV using the ATLAS detector at the LHC*, Eur. Phys. J. C **76** (2016) 653, arXiv: 1608.03953 [hep-ex].

[65] ATLAS Collaboration, *Optimisation and performance studies of the ATLAS b-tagging algorithms for the 2017-18 LHC run*, ATL-PHYS-PUB-2017-013, 2017, URL: https://cds.cern.ch/record/2273281.

[66] ATLAS Collaboration, *Performance of missing transverse momentum reconstruction with the ATLAS detector using proton–proton collisions at* $\sqrt{s} = 13$ *TeV*, (2018), arXiv: 1802.08168 [hep-ex].

[67] P. Z. Skands, *Tuning Monte Carlo Generators: The Perugia Tunes*, Phys. Rev. D **82** (2010) 074018, arXiv: 1005.3457 [hep-ph].

[68] P. Kant et al., *HatHor for single top-quark production: Updated predictions and uncertainty estimates for single top-quark production in hadronic collisions*, Comput. Phys. Commun. **191** (2015) 74, arXiv: 1406.4403 [hep-ph].

[69] G. Cowan, K. Cranmer, E. Gross and O. Vitells, *Asymptotic formulae for likelihood-based tests of new physics*, Eur. Phys. J. C **71** (2011) 1554, arXiv: 1007.1727 [physics.data-an], Erratum: Eur. Phys. J. C **73** (2013) 2501.

[70] M. Baak et al., *HistFitter software framework for statistical data analysis*, Eur. Phys. J. C **75** (2015) 153, arXiv: 1410.1280 [hep-ex].

[71] A. L. Read, *Presentation of Search Results: The CL(s) Technique*, J. Phys. G **28** (2002) 2693.